Marine CSEM synthetic study to assess the detection of CO_2 escape and saturation changes within a submarine chimney connected to a CO_2 storage site.

Naima K. Yilo[1]*, Karen Weitemeyer[1†], Timothy A. Minshull[1], Eric Attias[4], Hector Marin-Moreno[1,2], Ismael Falcon-Suarez[3], Romina Gehrmann [5], and Jonathan Bull [1]

[1] *School of Ocean and Earth Science, University of Southampton, UK*

[2] *Norwegian Geotechnical Institute, Norway.*

[3] *National Oceanography Centre, University of Southampton Waterfront Campus, Southampton, UK.*

[4] *Institute for Geophysics, Jackson School of Geosciences, The University of Texas at Austin, USA*

[5] *Dalhousie University, Canada*

† *Also at Ocean Floor Geophysics Inc., Burnaby, BC, Canada.*

SUMMARY

Carbon capture and storage (CCS) within sealed geologic formations is an essential strategy to reduce global greenhouse gas emissions, the primary goal of the 2015 United Nations Paris Agreement. Large-scale commercial development of geological CO_2 storage requires high-resolution remote sensing methods to monitor CO_2 migration during/after injection. A geologic formation containing a CO_2 phase in its pore space commonly exhibits higher electrical resistivity than brine-saturated (background) sediments. Here, we explore the added value of the marine controlled-source electromagnetic (CSEM) method as an additional and relevant geophysical tool to monitor moderate to significant changes in CO_2 saturation within a fluid conduit breaking through the seal of a CCS injection reservoir, using a suite of synthetic studies. Our 2D CSEM synthetic models simulate various geologic scenarios incorporating the main structural features and stratigraphy of two North Sea sites, the Scanner Pockmark and the Sleipner CCS site. Our results show significant differentiation of leakage through the seal with CO_2 saturation (S_{CO_2}) ranging between 20 and 50 per cent, while our rock physics model predicts that detection below 20 per cent would be challenging for CSEM alone. However, we are able to detect with our 2D inversion models the effects of saturation with 10 and 20 per cent CO_2 within a chimney with 10 per cent porosity.

We demonstrate that simultaneous inversion of E_y and E_z synthetic electric field data facilitates a sharper delineation of a CO_2 saturated chimney structure within the seal, whereas E_z synthetic data present higher sensitivity than E_y to S_{CO_2} variation, demonstrating the importance of acquiring the whole 3D electric field. This study illustrates the value of incorporating CSEM into measurement, monitoring, and verification (MMV) strategies for operating marine CCS sites optimally.

1 INTRODUCTION

The objective of the 2015 United Nations Paris Agreement is to limit global temperature rise to less than 2° C above pre-industrial levels by reducing greenhouse gas emissions and therefore promoting cleaner energy (UN Paris Agreement, 2015). The Sixth Assessment Report of the Intergovernmental Panel on Climate Change (IEA 2021) highlights that Carbon Capture and storage (CCS) is needed to compensate for CO_2 emissions from hard-to-abate industry sectors (e.g. agriculture, cement, aviation). Thus, CCS is necessary to curb global emissions to comply with the Paris Agreement targets. In Europe, private and public sectors are jointly developing CCS offshore projects. An example is the Northern Lights project, driven by three private companies and the Norwegian government (Furre et al. 2019). An extensive list of CCS projects, both onshore and offshore, at various stages of development, are detailed by Ringrose & Meckel (2019).

CO_2 can be sequestered into geological media (reservoirs) by: (1) injection into depleted oil and gas reservoirs; (2) injection into saline aquifers; (3) replacing methane in coal beds; (4) storage in salt caverns (Bachu 2000), or (5) mineralisation in mafic and ultra-mafic reservoirs (e.g., Goldberg et al. 2008). Depending on geothermal and pressure conditions, CO_2 can be stored as a gas, liquid, or supercritical fluid (e.g., Hoteit et al. 2019; Goldberg et al. 2008).

Depleted (sandstone) gas reservoirs or saline aquifers are ideal CCS sites because (1) they are superimposed by low-permeability cap rock, thus, providing a seal that prevents the upward migration of gas, (2) they are typically near infrastructure once used to extract oil/gas and, (3) they do not chemically react with CO_2. Offshore CO_2 storage in sandstone reservoirs has been successfully demonstrated in the North Sea, particularly in the Sleipner field, the world's first commercial CO_2 storage project (Baklid et al. 1996; Hansen et al. 2005). The CO_2 injected in the Sleipner reservoir, a saline aquifer at depths of around 800 m below the seafloor, is frequently monitored with seismic reflection methods (Chadwick et al. 2019).

Remote monitoring of CCS sites is key to understanding CO_2 containment during and after injection. CO_2 leakage from the injection reservoir to shallower depths or in the water column is a significant concern in CCS. Detecting and understanding CO_2 flow outside the storage reservoir at an early seepage stage is important in preventing unexpected CO_2 from causing acidification of bottom water, thus affecting marine life (Vielstädte et al. 2019), contaminating any freshwater reservoirs and for risk and liability management (Gasperikova et al. 2022).

Failure in the seal can create pathways for the migration of subsurface fluids to shallower depths. CO_2 injection may cause migration of fluids through pressure-induced fractures (Rutqvist et al. 2016), or by pressure changes within pre-existing fractures and sub-vertical conduits (also referred to as chimneys/pipes), which serve as leakage pathways (e.g., Robinson et al. 2021; Davies 2003). These

chimneys exist in the North Sea (Karstens & Berndt 2015) and globally (Cartwright & Santamarina 2015). We use the term chimney for sub-vertical fluid conduits or fluid escape features that are generally observed in seismic reflection data as seismic blanking zones (Karstens & Berndt 2015). In Sleipner, it has been shown that the CO_2 migrates vertically upwards from the reservoir injection point and intra-reservoir barriers (mudstones) through several relatively high-permeability chimneys. One particular chimney serves as the primary pathway for CO_2 upward migration (Chadwick et al. 2004, 2019; Williams & Chadwick 2021).

Seismic P-wave velocity (V_p) is a good indicator of fluid changes in the pore space of rocks. V_p in rocks with a high water saturation is particularly sensitive to gas (e.g. CO_2) present within the pore space; a small amount of gas (e.g. <5 per cent) would result in a significant decrease in the P-wave velocity because the effective bulk modulus of the pore fluid is then much smaller than the bulk modulus of water (Lee 2004). Therefore, V_p normally remains insensitive to high gas saturations but this depends on how the gas distribution within the pore space (Brie et al. 1995; Lee 2004) but generally V_p is very sensitive to low gas saturations (Domenico 1976). Electrical resistivity is very sensitive to changes in the fluid within the pore space because brine or saline water is very conductive (low resistivity) while gas has a high resistivity. Electrical resistivity is sensitive to porosity and the amount of brine present in the pore space. However, electrical resistivity is not sensitive to the disconnected gas that may be present in low saturations. Thus, measurements of V_p and electrical resistivity can be used in conjunction to quantify the non-aqueous fluid saturations.

1.0.1   *Marine CSEM - A viable technique to monitor CCS sites*

This study uses a marine CSEM system consisting of a deep-towed transmitter and seafloor receivers. The transmitter generates an electromagnetic (EM) field that diffuses through the seawater and seafloor. If the electromagnetic field propagates through a more resistive unit within the shallow seafloor, the electric field amplitude is less attenuated, which is measurable by towed or seafloor receivers. Previous studies have demonstrated that the CSEM method can pinpoint sub-seafloor vertical migration of resistive fluid phases (gases) (e.g., Goswami et al. 2016; Attias et al. 2016). Since CO_2 is electrically resistive, it can be detected by CSEM (Park et al. 2017; Ramirez & Friedmann 2008; Schmidt-Hattenberger et al. 2012). Onshore, electrical resistivity methods have been used to monitor CO_2 storage sites (Schmidt-Hattenberger et al. 2011; Streich et al. 2010). The use of CSEM monitoring has been modelled for oil and gas and geothermal applications onshore (e.g., Wirianto et al. 2010; Streich et al. 2010; Börner et al. 2015) and offshore (e.g., Orange et al. 2009). CSEM monitoring has been successfully implemented in onshore CCS sites (e.g., Girard et al. 2011), hydrocarbon production fields (e.g., Tietze et al. 2019) and geothermal fields (Bretaudeau et al. 2021).

Park et al. (2017) present results of a marine CSEM survey acquired after the start of CO_2 injection at the Sleipner field and discusses the benefits of monitoring CCS using time-lapse marine CSEM.

Seismic reflection repeats are commonly used to monitor CO_2 storage sites, also referred to as 4D or 'time-lapse' seismic surveys. Time-lapse seismic surveys are critical to monitoring the CO_2 plume migration at the Sleipner field in the North Sea (Chadwick et al. 2004, 2005, 2014, 2019). CSEM can complement the seismic reflection methods with information regarding the nature of the pore fluid and helps distinguish between fluid substitution, lithology, and mechanical effects. Therefore CSEM should be considered for reservoir integrity monitoring. The synthetic CSEM/seismic monitoring studies by Fawad & Mondol (2021) and Dupuy et al. (2021) show that both methods are required to monitor CO_2 storage adequately. Nearly all published studies on time-lapse CSEM conclude that monitoring the subsurface with CSEM is feasible (e.g., Girard et al. 2011; Tietze et al. 2019; Bretaudeau et al. 2021). CSEM studies using both synthetic data (Fawad & Mondol 2021; Gasperikova et al. 2022; Gehrmann et al. 2021a) and real data (Schmidt-Hattenberger et al. 2011) infer that CSEM methods can monitor CO_2 storage sites. Fawad & Mondol (2021) present a CSEM synthetic study in the Norwegian North Sea, combining time-lapse marine CSEM and reflection seismic while Gasperikova et al. (2022) discusses the sensitivities of gravity, EM, and seismic to detect CO_2 migration outside of the reservoir (secondary plumes) for onshore CCS sites. Schmidt-Hattenberger et al. (2011) discuss the benefits of employing time-lapse CSEM to monitor the Ketzin (Germany) onshore CCS site. Dean & Tucker (2017) suggested that changes in resistivity associated with CO_2 injection sites are close to or below the detection limits for time-lapse CSEM, but no supporting model or data are presented.

The sensitivity of the CSEM method to various resistivity contrasts due to CO_2 leakage within known background geology can be derived from synthetic studies. In this work, we conduct a suite of synthetic studies to determine the marine CSEM method sensitivity to various CO_2 leakage scenarios through a chimney structure connected to a CO_2 storage reservoir. We combine two sites, both associated with seismic chimneys, in a synthetic model study: the Scanner pockmark in the North Sea, representative of the seal breached by a chimney connected to a pockmark vent system; and the Sleipner CO_2 injection site, used as a saline aquifer analogue for CO_2 injection. To our knowledge, this is the first study to examine CSEM's capability to monitor CO_2 leakage via a fluid conduit within a clay-rich overburden. Gasperikova et al. (2022) analyse CO_2 plumes outside of the reservoir and we expand this work by considering rock physics of a clay-rich overburden and a fluid conduit. The importance of reservoir flow models in CCS and their integration with geophysical monitoring has been discussed in Commer et al. (2022), who used a simplified approach to constrain EM inversions applying the fluid saturation predicted from the flow modelling. We used a similar approach to interpret our CSEM modeling results in the context of CSEM monitoring. We applied realistic saturation scenarios modelled

with guidance from the multi-phase fluid flow modelling and saturation distribution, considering the escape of CO_2 via a chimney at Scanner pockmark site (Marín-Moreno et al. 2019).

2   GEOLOGIC SETTING

The Scanner pockmark is an active gas vent complex in the south of UK's license block 15/25 located at 58°16'54.0 "N, 0°58'14.6 "E (Figure 1) in ∼155 m of water (Gafeira & Long 2015). A chimney structure interpreted below the Scanner pockmark is known to function as a fluid conduit that reaches the seabed (Karstens & Berndt 2015; Robinson et al. 2021; Böttner et al. 2019). In the case of the Scanner pockmark, the migrating fluid is methane and not CO_2, but the structure and shallow clay-rich stratigraphy serves as an analogue to study leakage pathway structures within the modeled seal connecting a CO_2 reservoir with the seafloor. Li et al. (2020) calculated the current methane flux from the Scanner Pockmark into the water column to be between 1.6 x 10^6 kg/year and 2.7 x 10^6 kg/year (272-456 L/min), from active acoustic inversion imaging. Callow et al. (2021) provides an overview of geophysical surveys performed in this site.

The Sleipner CO_2 injection site, located in the Norwegian North Sea, has a seal characterized by thin layers of clay, as indicated by high gamma-ray intensity (Chadwick et al. 2005, Figure 2). We also examine the Sleipner site as an analogue for our model. We use the Sleipner injection reservoir, a saline aquifer where CO_2 is sequestered, and the deep seal stratigraphy immediately above it to complement our Scanner pockmark seal model, which covers the shallower seal. Both the Scanner and Sleipner sites have similar Neogene to Quaternary stratigraphy (Figure 1b and Figure 2). The Scanner and Sleipner Quaternary sediments (∼400 m thick) are composed of fine-grained material (silt and clay) as described by Stoker et al. (2011). This Quaternary succession is underlain by the ∼600 m thick Nordland Group (NG), a sequence of Neogene age claystone inter-bedded with limestone and the Utsira sandstone (Judd et al. 1994), referred as the Utsira reservoir in this manuscript. At Sleipner, the Utsira reservoir is ∼800–1000 m deep and ∼200–300 m thick. The clay-rich seal above the Utsira reservoir is several hundred meters thick, divided into three units (Zweigel et al. 2004, Figure 2) that are referred to as the geological seal throughout the manuscript. The lowest part of the seal, also known as the 'Shale Drape', forms a clay-rich basin-restricted unit within the Utsira formation itself (Chadwick et al. 2002). Above this resides the thick Pliocene succession, the Nordland Group, also called the 'middle seal' (Chadwick et al. 2002). The 'middle seal' is comprised mainly of prograding units, dominantly clay in the basin centre and coarsening into sandier facies both upwards and towards the basin margins (Stoker et al. 2011). The uppermost section, the 'upper seal,' is comprised of the

Quaternary clay-rich glaciomarine and glacial tills sequence from the Aberdeen Ground (AG), Coal Pit (CP), and Witch Ground formations (WG) (Chadwick et al. 2002).

3 METHODS

3.1 Rock physics

Rock physics models are used to estimate the expected resistivity for a given CO_2 saturation for the seal properties of the Scanner pockmark and the CO_2 injection reservoir at Sleipner. Our model scenarios assume that CO_2 is injected at a saline aquifer with the same properties as the Utsira formation, reaching S_{CO_2} = 50 per cent and escapes through a chimney within a clay-rich seal with various CO_2 saturations. For comparison following (Constable 2010), we also estimate P-wave velocity for a 'patchy gas model' from Lee (2004), using a confining pressure of 2.59 MPa to 18.21 MPa from top to base seal, calculated using the geological thickness and rock properties from the hybrid Sleipner/Scanner geological model. We calculate temperatures of 17.8 °C for the seal and 37 °C for the reservoir using a North Sea geothermal gradient of 30°C/km (Shell-UK-limited 2014).

The electrical resistivity for the sandstone reservoir is estimated using Archie's Law (Archie 1942), while the resistivity for the seal composed of clay-rich silty sediments is derived from Waxman Smits Juhasz shaley-sand model (Juhasz 1981; Appendix A). Appendix A discusses Archie's and Waxman-Smits equations, derivations, parameters, and their implementation to calculate the resistivity and partial water saturation of clay-rich sands from well-logs. The empirical relationship proposed by Archie (1942) relates the bulk electrical resistivity of a geological formation in the subsurface (ρ_0) (saturated with any fluid) with its porosity (ϕ), pore fluid resistivity (ρ_w) and fluid saturation (S_w), as follows:

$$\rho_0 = a\rho_w\phi^{-m}S_w^{-n} \tag{1}$$

where a is the tortuosity coefficient, m is the cementation exponent, and n is the saturation exponent.

Archie's equation is not adequate for sediment, where conductive clay minerals are present (Wyllie & Gregory 1953). In clay-rich sands, an excess of ions around clay particles generate additional conduction pathways along the clay surface, and the electrical resistivity of the clay surface depends on the brine conductivity in a non-linear manner (Mavko et al. 2009). This conduction occurs in addition to the diffusion of natural ions through the bulk pore fluid. As a result, the resistivity of clay-rich sand for partially brine-saturated formation (ρ_t) is lower than that of clean sand with the same porosity and water saturation (Juhasz 1981). The resistivity equation considering the clay effect by Waxman & Smits (1968) is shown below:

$$\rho_t = \left[\frac{a\rho_w}{\phi^m S_w^n (1 + \frac{\rho_w}{B} Q_v S_w)}\right] \tag{2}$$

where B is the equivalent cation conductance, which is dependent on temperature and salinity (Equation A.7, Appendix A) and Q_v is the cation exchange capacity (CEC) per unit volume (Equation A.6, Appendix A).

To obtain Q_v, the total pore volume and CEC must be known from core measurements (Appendix A, Equation A.6). The normalized Waxman–Smits-Juhasz equation (Juhasz 1981) removes the need to measure the CEC from cores as it uses V_{SH} (volume of shale) derived from well-logs, such as the gamma-ray or density-neutron logs. This is given below, after isolating ρ_t from Equation A.14 in Appendix A:

$$\rho_t = \frac{aS_w^{-n}\phi^{-m}}{\left[\frac{1}{\rho_w} + \frac{V_{SH}\phi_{SH}}{\phi}\left(\frac{a}{\rho_{SH}\phi_{SH}^{m} - \frac{1}{\rho_w}}\right)S_w^{-1}\right]} \tag{3}$$

where ϕ_{SH} is the total shale porosity and ρ_{SH} the resistivity of the formation with 100 per cent volume of shale (V_{SH}); while m and a are the cementation and tortuosity exponents for the clay-rich formation. See Equation A.6 to Equation A.14 in Appendix A for more details).

We estimated V_{SH} from the gamma-ray log data for well 15/09-13 at Sleipner (Park et al. 2011, Figure 2b) by linearly interpolating (GR_{log}) between the minimum (GR_{min}) and maximum (GR_{max}) values, as follows:

$$V_{SH} = \frac{GR_{log} - GR_{min}}{GR_{max} - GR_{min}} \tag{4}$$

The gamma-ray log responds to the number of radioactive minerals (e.g., potassium, uranium, and thorium) contained within the rocks adjacent to the borehole (Brannon & Osoba 1956). This log is used as an indicator for the presence of clay because formations rich in clay show a high radioactive count, while sands are characterized by low radioactive content and a low gamma-ray count (Brannon & Osoba 1956).

We used the range 11-103 gAPI to estimate V_{SH}, based on the clean rock at 2500 mbsf (GR_{min}) and the shale formation at 2910 mbsf (GR_{max}), respectively (Figure 2b). The resistivity corresponding to 2910 mbsf depth (Figure 2d) was used as the resistivity of the 'clay-rich' formation (ρ_{SH} = 4 Ωm).

Finally, Arp's Law (Equation B.1, Appendix B) is used to determine the pore water resistivity (ρ_w) within the Scanner pockmark. Arp's Law extrapolates the pore water resistivity from a known pore water resistivity (ρ_w) and temperature at a depth using the geothermal gradient of the area of interest (Arps 1953).

3.2 Model scenarios

In order to understand the effect of a chimney isolated from any fluid changes in CO_2 saturations we modelled a simplified layered model using the rock physics properties of the Scanner pockmark for the seal and the properties of Sleipner field for a saline aquifer reservoir underneath it and a chimney that cross-cuts the seal. We considered synthetic modeling scenarios before the CO_2 injection starts (Figure 3a) and after injection (Figure 3b-e and Figure 4). We considered the reservoir saturation with brine only before injection (i.e., a saline aquifer) and a reservoir partially saturated with CO_2 after injection. The effect of fractures within the chimney was modeled by giving a 10 per cent higher porosity to each layer within the chimney bounds (Figure 3a).

For all our scenarios, the resistivity for the Utsira formation (target site) before injection ($S_w = 1$) and after injection ($S_{CO2} = 0.5$) was determined with Archie's empirical relationships (Section 3.1, Appendix A), using the properties from Table 1. The Utsira sand Archie's parameters: $m = 1.6$, $a = 1.1$ and $n = 1.8$ are selected based on Mavko et al. (2009) and confirmed by laboratory studies performed on CO_2 saturated Utsira sand samples (Falcon-Suarez et al. 2018; Alemu et al. 2013). For the sealing formation, the resistivity within and outside the chimney for the different saturation scenarios, before and after the injection started, was determined using the Waxman-Smits-Juhasz shaley-sand model (Section 3.1, Appendix A) using the properties listed for each formation on Table 1. The seal Archie parameters used were $m = 1.8$, $a = 0.9$ and $n = 2$ (Table 1), consistent with observations of clay-rich shallow marine sediments (Riedel et al. 2006; Mavko et al. 2009).

In order to understand the resistivity changes in the chimney within the seal and the detectability of potential leaks through it we considered a chimney fully saturated with brine that cross-cuts the seal and is connected to a CO_2 reservoir saturated with 50 per cent CO_2 (Figure 3b). Then we consider three scenarios where a leak through the chimney has occurred and this results in a chimney saturated bottom to top with 1) 10 per cent CO_2 (Figure 3c), 2) 20 per cent CO_2 (Figure 3d) and 3) 50 per cent CO_2 (Figure 3e). All these scenarios consider injection that has occurred in a saline aquifer for some time, and the reservoir has reached a saturation of 50 per cent CO_2. We also analysed the changes in CO_2 saturation within the chimney due to the evolution of a leak through time. Two scenarios were considered with saturation variation within the chimney that correspond to 5 years and 25 years after injection (Figure 4b-c), according to the flow modelling results of Marín-Moreno et al. (2019) for the Scanner pockmark area (analogue for the seal). The flow model assumes that the CO_2 in the reservoir is connected to the chimney and migrates upwards primarily through connected micro-fractures within the chimney. The volume of such micro-fractures within the chimney is likely to be a small proportion of the total pore volume of the chimney. Hence, even if the micro-fractures become fully saturated with CO_2, the CO_2 saturation averaged over the total pore volume of the chimney is likely smaller

than that in the reservoir. We implement realistic saturation changes and fluid distribution through time by using the same overburden layer thickness, porosities, and rates of CO_2 propagation within the chimney as Marín-Moreno et al. (2019).

3.3   Marine CSEM system and 2D synthetic models

In CSEM synthetic studies, the true resistivity model of the subsurface is assumed to be known. By varying either the electrical resistivity, due to geologic properties, or the survey line parameters (e.g., transmitter-receiver geometry, frequency), we can examine the feasibility of using specific CSEM se-tups to resolve variations of the electrical resistivity in the seafloor.

This study uses a marine CSEM system comprising a deep-towed horizontal electric dipole (HED) transmitter and ocean-bottom electric field (OBE) receivers. The model study is based on the transmit-ter and receiver geometry from profile 2 (Figure 5b) of the Scanner pockmark (Figure 5a) (Gehrmann et al. 2021b). Therefore, while the modelling considers realistic acquisition parameters designed to investigate a realistic geologic scenario, our study is limited to what this particular survey geometry is capable of detecting, in regards to CO_2 saturation within the modelled chimney. A suite of synthetic forward models were generated with added Gaussian noise, and multiple inversions were run to simu-late various fluid saturations within a chimney structure. We inferred changes in fluid saturation across the chimney, from the resulting resistivity inversion model, using two rock physics models (Archie 1942; Juhasz 1981) as described in Sections 3.1.

During the survey along profile 2, the transmitter was towed 20-40 m above the seabed and transmitted a 1 Hz, 100 Ampere square wave (Gehrmann et al. 2021b). The transmitter passed six OBE receivers spaced 500 m apart along the 7 km long profile, resulting in 213 unique transmitter-receiver geome-tries (Figure 5). We modelled CSEM data with 1 Hz fundamental frequency and the higher amplitude harmonics 3, 5, 7, 9, and 11 Hz observed in the CSEM data (Appendix C). Both the horizontal (inline - aligned with towline direction, E_y) and vertical (E_z) electric field components were modelled for all frequencies and transmitter-receiver geometries.

The synthetic data for the CSEM system and navigation parameters as described above were generated using MARE2DEM (Key 2016), a parallel adaptive finite element code for 2D forward and inverse modelling of electromagnetic data. The data were contaminated with 4 per cent random Gaussian noise. The 4 per cent value is based on the data quality of the CSEM survey at Scanner. Similarly, the noise floor (inferred from the Scanner CSEM survey) was set to 10^{-13} V/Am^2 for both vertical and in-line components. Our 2D model includes an insulating air layer, a stratified seawater layer with a vari-able resistivity profile, and a seabed layer. The interface between the seafloor and water layer (seafloor

bathymetry) is generated by using the measured transmitter depth and altitude data (Gehrmann et al. 2021b) for the survey profile 2 (Figure 5). An air resistivity of 10^8 Ωm was used while the seawater resistivity was derived from the CTD (conductivity, temperature, depth) sensor-operated during the STEMM-CCS survey, a CSEM experiment at Scanner (Robinson et al. 2021) and ranges from 0.273 to 0.2777 Ωm at 20 to 160 m water depth. At this location, the changes in seawater resistivity with depth are insignificant. However, previous studies have demonstrated that an accurate seawater resistivity profile has a significant effect in recovering geologically plausible subsurface resistivity (e.g., Key 2009; Attias et al. 2020). The resistivity of the seafloor model was calculated as described in Section 3.1 using the input parameters from Table 1. The seafloor model consisted of six layers based on the stratigraphy described in Section 2 (Figure 2). Thicknesses as reported by Judd et al. (1994) were used for the Witch Ground and Aberdeen Ground formations (Table 1). Depth converted seismic reflection data from the Chimney experiment (Bull et al. 2018) were used to estimate the thickness for the Coal Pit and Ling Bank formations (Callow 2021). The Nordland group seal and the Utsira sandstone thicknesses are from Chadwick et al. (2004). A 500 m wide chimney was modelled, which cuts the stratigraphy from the top of the Aberdeen Ground formation at 400 m below seafloor (mbsf) to the Utsira formation at 1000 mbsf, using the Chimney's position/width observed in seismic reflection section (Figure 1b). An air resistivity of 10^8 Ωm was used while the seawater resistivity was derived from the CTD (conductivity, temperature, depth) sensor-operated during the STEMM-CCS survey, a CSEM experiment at Scanner (Robinson et al. 2021) and ranges from 0.273 to 0.2777 Ωm at 20 to 160 m water depth. At this location, the changes in seawater resistivity with depth are insignificant. However, previous studies have demonstrated that an accurate seawater resistivity profile has a significant effect in recovering geologically plausible subsurface resistivity (e.g., Key 2009; Attias et al. 2020). The resistivity of the seafloor model was calculated as described in Section 3.1 using the input parameters from Table 1.

3.4 Inverse model parameterization

The CSEM inversion starting model used a 1 Ωm half-space resistivity for the sub-surface. The inversion allowed subsurface resistivity to vary, whereas the air and stratified seawater resistivity structures were fixed parameters. A quadrilateral mesh was constructed within the survey area (Key 2016), starting at the seafloor (minimum mesh is 10 m thick by 50 m wide) and up to 2000 m depth with a height growth ratio of 1.05, which corresponds to a thickness of 500 m at 2000 m depth, and a horizontal to the vertical smoothing ratio of 3. We used a triangular mesh outside the discretized quadrilateral mesh, with cell size increasing with distance from the survey area. The inversion starting model mesh

had $\sim$12000 free parameters.

First, a series of unconstrained inversions are run from a 1 Ωm half-space starting model using synthetic electric field data (contaminated with noise) generated from 2D forward models of the reservoir before and after CO_2 injection, with a homogeneous chimney saturation. Second, constrained inversions were generated with 2D synthetic data for scenarios after injection with variable CO_2 saturations within the chimney. This was achieved by placing penalty cuts at the top and base of the injection reservoir with a weight of 0.1. Penalty cuts allow for 'rough' changes in resistivity, eliminating the inversion algorithm's preference to smooth interfaces. MacGregor & Sinha (2000) present real CSEM data examples where seismic and geological data are incorporated to constrain the depths of structural boundaries. A priori information (e.g. seismic horizons or geological information) help guide the inversion toward yielding resistivity models that are consistent with other data sets and knowledge from the area of interest. In CCS projects, where the boundaries of the injection reservoir are known from seismic reflection data, constraining the reservoir can improve CSEM inversions.

4   RESULTS

4.1   Rock physics results

Since our objective is to investigate the detectability of a CO_2 leak or plume outside of the injection reservoir, two rock physics relationships (Archie's and Waxman-Smits-Juhasz's) are compared to construct a resistivity model of the clay-rich formations that we are modelling as the seal. Both Archie's and Waxman-Smits-Juhasz's relationships predict similar saturations for a given resistivity in the Witch Ground and Coal Pit clay-rich formations (Figure 6). These two formations have a higher porosity than the deepest clay-rich formations, the Aberdeen Ground and Nordland Group (Table 1). The saturations predicted by Waxman-Smits-Juhasz for the deepest clay-rich formations (Aberdeen Ground and Nordland Group) are 1.5 to 2.5 times higher than those predicted with Archie's law, given the same bulk resistivity value.

A comparison of the seal and reservoir CO_2 saturations shows that the same resistivity value in the seal and reservoir results in a different CO_2 saturation due to different rock physics relationships used to represent the reservoir and the seal. Apart from different rock physics models, we considered the geology, clay content, and porosity of each formation. The discrepancy observed between each layer/formation is driven primarily by differences in clay content and porosity. The differences between Archie's and Waxman-Smits-Juhasz models per formation (Figure 6) show the importance of employing a rock physics model for a clay-rich seal that considers the additional surface conduction pathways around the clay particles.

In Figure 7 we compare the P-wave velocity and resistivity against gas saturation, using a similar approach to Constable (2010) and references within. The largest change in acoustic P-wave velocity occurs for the first few percent of CO_2 saturation and, as the saturation increases, the velocity response changes very little. In contrast, there is little change to the electrical resistivity for the CO_2 saturation below 20 per cent but a rapid increase of electrical resistivity is observed at CO_2 saturations higher than 20 per cent.

4.2   Detectability of CO_2 saturation changes on 2D CSEM synthetic data

The anomaly due to CO_2 escaping through the chimney was computed using the amplitude percentage difference for two models with a chimney connected to the CO_2 reservoir saturated with 50 per cent CO_2 and : 1) a chimney saturated with 10 per cent CO_2 (Figure 3c) and 2) a chimney saturated with 20 per cent CO_2 (Figure 3d). The percentage difference is obtained by calculating the difference with a model of a chimney with no CO_2 (S_{CO_2}=0 per cent) and the reservoir saturated with 50 per cent CO_2 (Figure 3b).

Considering a noise floor at 10^{-13} V/Am^2, as observed in the STEMM-CCS data, the E_z anomaly for a 20 per cent saturation ranges between 20 and 60 per cent amplitude percentage difference while the E_y anomaly ranges between 10 and 30 per cent amplitude percentage difference, with the highest response at 9-11 Hz. The anomaly for E_y and E_z for the two CO_2 saturated models with 20 per cent CO_2 (Figure 8) and 10 per cent CO_2 (Figure A2, Appendix D) is higher in percentage difference than the random noise modelled (4 per cent) and above the instrument noise floor, meaning that both are detectable.

For the E_z model with S_{CO_2} = 20 per cent the amplitude anomaly for one receiver (receiver OBE-D) exists at a narrower range of offsets for the higher frequencies (5-11 Hz). This anomaly occurs at shorter source-receiver offset ranges, only (700-1500 m). For 1-3 Hz frequencies, the anomaly occurs at higher source-receiver offsets (2000-3000 m, Figure 8a). For one of the OBE receivers (OBE-D), the E_y amplitude anomaly at frequencies of 5-11 Hz occurs at a source-receiver offset of 700–1500 m, while for 3-5 Hz the anomaly is at 1200-1700 m. At frequencies of 1 to 3 Hz, the anomaly is much broader and extends from 1200 m to 3900 m offset (Figure 8a and b). For the frequencies inverted in this study (1-11 Hz), the electric field amplitude anomaly of a CO_2 plume with 20 per cent saturation is more prominent as frequency increases in both the E_z and E_y components (Figure 8). However, the anomaly in E_z is of higher amplitude than in E_y.

4.3 Synthetic inversion results of the chimney structure

Our suite of synthetic inversions with 4 per cent data error, converged to an RMS misfit of $\sim$1.0. Normalized residuals for our inverted values are within 4 per cent for the amplitude and phase of the E_y (inline) and E_z (vertical) electric field (E-field) components. Figure A4 (Appendix F) shows an example of E_y and E_z electric field data for an ocean bottom instrument (OBE) at a fundamental frequency of 1 Hz.

Our synthetic modelling considered a 10 per cent more porous chimney (Figure 9d), due to connected fractures, compared to the background geology (Figure 9a). The model of Figure 9d represents a stage before CO_2 injection has started. This model would generally be called the 'baseline' survey of a monitoring CCS project, which provides a reference point to analyse CO_2 changes within the reservoir and overburden through the life of a CCS project. In the following sections, we analyse the detectability of a CO_2 leak through a chimney with CSEM and not the changes in saturation within the reservoir. Hence, we do not compare our CO_2 saturated models with this 'baseline' model but rather with the model with 0 per cent saturation within the chimney and 50 per cent within the reservoir (Figure 3b).

Even when the model of the chimney in Figure 9d is not strictly the baseline for our study of the seal, we consider it relevant to understand the resistivity structure and the expected CSEM anomaly related to the chimney only. CO_2 injection time-lapse analysis of resistivity models requires a thorough investigation of the resolution and model characteristics at different stages and understanding of the underlying geology. Analysing the signal related to a chimney only (before CO_2 injection) is essential for detecting and monitoring a leak through a chimney and interpreting resistivity inversion results related to this.

The E_y and E_z inversions of the model in Figure 9d show a visible response to a 10 per cent porosity perturbation inside a chimney cutting through a stratified subsurface (Figure 9d-f), which resulted in a conductive anomaly contrasting from the background sediments (Figure 9a-c). The synthetic inversion model results using the inline and the vertical electric field data adequately delineate the conductive chimney structure (Figure 9d-f).

We analyse the electrical resistivity inversion of the conductive chimney also by looking at resistivity profiles extracted from our 2D inversion at a model distance of 3.8 Km. The resistivity profile for the E_z 2D inversion detects the chimney's resistivity range of 1.6-1.9 Ωm for the Aberdeen Ground formation and 1.9 to 2.1 Ωm in the Nordland Group (Figure 10b). The inversion using E_y data presents a similar resistivity range for these formations (Figure 10a). We derived the porosity from the inverted resistivity profile to analyse the sensitivity of our inversion models (Figure 10d). For the the clay-rich interval, we derived the porosity profile for the inverted resistivity for E_y, E_z and $E_y E_z$, using the

Waxmann-Smits-Juhasz approach (Equation 3). For the reservoir we derived the porosity profile using Archie's equation (Equation 1). The porosity of the Aberdeen Ground formation (Table 1, $\phi = 0.22$), composed mainly of clay, can be derived from the resistivity of the E_z and E_y components separately, producing porosity values of 0.19-0.25 from both components when inverted separately (Figure 10d). The simultaneous $E_y E_z$ inversion of the chimney produces a sharper resistivity and porosity model than the inversion of individual E-field components. For example, the porosity of the Aberdeen Ground formation ranges from 0.2 to 0.21 when E_y and E_z are inverted jointly (Figures-10d).

4.3.1 S_{CO_2} scenarios - Unconstrained inversions

We explored the potential of marine CSEM to differentiate between three scenarios of CO_2 reservoir leakage via the electrical resistivity response. The models considered assume different CO_2 leakage scenarios through a chimney in the overburden connected to a CO_2 reservoir. A constant saturation of 50 per cent CO_2 was modeled within the reservoir while saturation changes were modelled within the chimney. Three saturations from bottom to top of the chimney are considered in our sensitivity analysis: 10, 20, and 50 per cent of CO_2.

Our models show that both the E_y and E_z electric field components are sensitive to such CO_2 saturations (Figure 11). However, in all scenarios, the E_z component resolves the true model features with better resolution than E_y. At S_{CO_2} = 10 per cent, the E_y and E_z inversions indicate a small resistivity change at the chimney location that requires knowledge of the true model to interpret it as a saturation change (Figure 11a, b, and c). At S_{CO_2} = 20 per cent, E_y and E_z inversions (Figure 11b, c, and d) detect the chimney structure, with 50 m to 100 m deviations from the true model (Figure 11d-f). When S_{CO_2} = 50 per cent, both E_y and E_z sharply resolve the overall chimney structure (Figure 11g, h and i). At the chimney edges, the resistivity anomaly from the E_y inversion is lower than in the true model ($\sim$ 2.8 Ωm vs. 5 Ωm), 50 m wider at the top, and 150 m thinner at depth near the reservoir (Figure 11h). In comparison, the E_z inversion presents sharper chimney edges, with a resistivity of $\sim$ 3.5-4 Ωm at the edges, consistent with a width of $\sim$ 505 m and the chimney is marginally wider when closer to the reservoir ($\sim$ 510 m). (Figure 11i).

$E_y E_z$ inversion of the 10 per cent saturation scenario did not resolve the chimney location and width (Figure 12b), similar to when the components were inverted individually. The resistivity at the chimney for the AG formation was predicted to be around 2 Ωm versus 1.9 Ωm in the true model, corresponding to saturations between 0 and 10 per cent (Figure 13c and d) using the Waxman-Smits-Juhasz relationship (Equation-A.10). For the 20 per cent saturation case, when inverting E_y and E_z jointly, the width of the chimney is 450 m, which is more accurate than when these components are inverted individually. The chimney's width is taken at an intermediate depth, halfway from its base. Note, the

true width of the chimney is 500 m. The resistivity at the top of the chimney for the Aberdeen Ground formation is predicted to be 2.4 Ωm vs. 2.18 Ωm true model, corresponding with CO_2 saturations from 10 to 20 per cent (Figure 13f and g).

For the 50 per cent CO_2 saturation model, the simultaneous inversion using both E_y and E_z data accurately recovers the lateral extent of the top 300 m of the chimney while the bottom 500 m is less well resolved. The resistivity in the chimney for the Aberdeen Ground formation recovered by this inversion varies from 2.5 to 5.4 Ωm compared with 4.8 Ωm in the true model, corresponding to 35-50 per cent CO_2 saturation (Figure 13j and k) calculated using Equation-A.10.

4.4   Inverted resistivity and predicted CO_2 saturations.

We compared the predicted resistivity from an inversion with the true model for the various model scenarios by extracting resistivity profiles at the chimney center. We also calculate the corresponding CO_2 saturation (S_{CO_2}) of the various chimney seals for each extracted resistivity profile. For this calculation we used Equation A.10, the normalized Waxman and Smits's equation (Juhasz 1981), and the parameters in Table 1.

For the model with 10 per cent S_{CO_2}, a vertical profile extracted from the chimney centre in the E_y inversion has resistivity of $\sim$1.6-2.1 Ωm, which corresponds to an Aberdeen Ground formation S_{CO_2} of 0-15 per cent (Figure 13a). The E_z inversion has a sharper vertical resistivity profile for the Aberdeen Ground formation, ranging between $\sim$1.7 and 2 Ωm, corresponding to S_{CO_2} of 0-10 per cent (Figure 13b).

When the chimney is at an S_{CO_2}=20 per cent, the seal resistivity profile from the E_y inversion is smoother than the one from the E_z inversion (Figure 13d,e). E_y predicts a resistivity range of $\sim$1.8–2.4 Ωm as opposed to the 2.18 Ωm (Table 2) for the Aberdeen Ground formation, corresponding to 10-20 per cent CO_2 saturation. E_z inversions suggest that the Aberdeen Ground formation resistivity varies from $\sim$1.8 to 2.2 Ωm, which corresponds to 10-20 per cent calculated saturation S_{CO_2} for this resistivity.

At S_{CO_2} = 50 per cent, the resistivity from the E_y inversion is smoother (Figure 13h) though less sensitive to the chimney structure in comparison to the resistivity from the E_z inversion (Figure 13i). In the Aberdeen Ground formation, the E_y inversion has a resistivity of $\sim$ 2-5 Ωm (30-50 per cent S_{CO_2}) instead of 4.3 Ωm; comparable to the E_z inversion ($\sim$2.5–5 Ωm, $\sim$25–50 per cent CO_2).

4.4.1   A S_{CO_2} gradient within the Chimney - constrained inversions

CO_2 leakage through the chimney was modelled at two different times, 5 years and 25 years after the CO_2 reaches the base of the chimney. Here, the primary focus is on the detectability of CSEM to CO_2 and porosity-induced resistivity changes within the chimney. Therefore, a constant CO_2 saturation of 50 per cent was assumed in the reservoir. While the CO_2 saturation in the reservoir will vary in space and time, during and after CO_2 injection operations, it remains fixed for this study, thus focusing on the seal leakage and not the reservoir. The porosity distribution and the vertical changes in CO_2 saturation in the chimney are guided by Marín-Moreno et al. (2019) multi-phase reactive transport simulation of CO_2 leakage at the Scanner Pockmark.

At 5 years (Figure 4b), the first 100 m from the bottom of the chimney ($\sim$800-700 mbsl) has 20 per cent CO_2 saturation followed by a 150 m section with 15 per cent CO_2 (up to $\sim$550 mbsl) and the rest saturated with brine. In this model, we allow a resistivity discontinuity across the reservoir boundaries (constrained inversion), which enhances the differentiation between resistive (CO_2 saturated – deep chimney) and conductive (brine saturated – shallow chimney) regions. The variable saturation can be differentiated in the inversion (Figure 14b-c).

At 25 years (Figure 4c), the first 100 m from the bottom of the chimney ($\sim$800-700 mbsl) are saturated with 35 per cent CO_2 followed by a 150 m section with 25 per cent CO_2 saturation ($\sim$550 mbsl), a 200 m section with 20 per cent CO_2 saturation (up to $\sim$350 mbsl), and the rest saturated with brine. The E_y component resolved the chimney's CO_2 saturated layers (true model features) with better lateral and vertical resolution than E_yE_z combined. We constrained these inversions by enforcing penalty cuts of 0.1 (Key 2016) to the base and top of the reservoir layer at 800 and 1000 m depth. Constraining the reservoir enhanced the E_y response. The inversion model for E_yE_z at 25 years (Figure 14f) captures well the upward migration of CO_2 through the chimney so that the resistor that emerges from the reservoir is more elongated compared to the model at 5 years (Figure 14c).

The constrained inversions at 5 and 25 years show distinctive (time-dependent) detectable differences in the chimney's height and resistivity. In bothscenarios, the chimney's brine-saturated (S_{CO_2}=0 per cent) upper regions are well-resolved by our constrained synthetic inversions (Figure 14).

5   DISCUSSION

We have explored the added value of using marine CSEM to detect upward CO_2 migration through sub-vertical fluid escape/chimney structures. Comparing the P-wave velocity and resistivity of our model area as a function of gas saturation (Figure 7), similar to Constable (2010), the benefit of coupling CSEM and seismic methods for monitoring CO_2 leakage becomes evident. Combining CSEM

and seismic methods allows one to distinguish clearly if a leak is significant because CSEM will present a significant signal when saturations exceed 20 per cent while seismic velocities may remain almost constant at this stage of saturation. Seismic velocities are highly sensitive to saturations below 10 per cent, whereas resistivity shows only a gradual response to saturation increases between 10-20 per cent.

Our results show that there is a distinct difference between inversion models with 0 and 10 per cent CO_2 saturation and 10 and 20 per cent CO_2 saturation within the modeled chimney. However a chimney with 10 per cent saturation is not clearly detectable in the regularised 2D inversions (Figure 11b-c and Figure12b) when comparing its response with that of the background sediments. However, the inversion of a chimney with 20 per cent saturation is clearly detectable (Figure11e-f and Figure12d). When comparing 2D CSEM synthetic data for a model with a chimney saturated with 10 per cent CO_2 (S_{CO_2}=10 per cent) with the background sediments (S_{CO_2}=0 per cent) the resistivity contrast is too small to be detected with CSEM (Figure A3, Appendix D). However, when we compare 2D synthetic data between a model with a chimney after injection and before a leak with a chimney with 10 per cent CO_2 we observe an amplitude percentage difference of 10-20 per cent in E_y and 25-40 per cent in E_z in the synthetic data (Figure A2, Appendix D). This signal seems large enough in E_z data for one receiver but is not detectable in the inversion results. We believe that using the survey geometry and rock physics applied here we are able to detect with confidence a CO_2 leaks of saturation below 20 per cent and the detection limits with our inversion modelling are somewhere between 10 and 20 per cent saturation. These results may also imply that if a chimney or conduit has a smaller porosity than what we modeled a saturation of 10 per cent may not be detectable in CSEM data. Consequently, similar to Gasperikova et al. (2022), we consider our detection threshold potentially valid for an analogue area in the North Sea, with comparable boundary conditions (i.e., water depth, injection depth), geology and rock physics properties, concurring with Gasperikova et al. (2022) notion that the detection limits of CSEM for CO_2 leaks are site-specific.

Seismic velocities are extremely sensitive to low CO_2 saturations (e.g., below 10 per cent), which makes seismic methods a powerful tool to detect any type of seepage at an early stage. However, as the seismic velocities normally have little sensitivity to changes above a 10 per cent saturation they fail to quantify the degree of saturation for values above this saturation. Therefore, the seismic method will be limited in certain CO_2 injection scenarios especially monitoring the CO_2 plume in a depleted gas reservoir. CSEM methods determine saturation changes above the seismic-based limits of around 10 per cent saturation. Hence, CSEM complements the seismic methods in the quantification of CO_2 saturation and in assessing the amount of CO_2 that has traveled within and from the reservoir. The value of this quantification depends on what CO_2 saturation limits within the seal regulators will al-

low for and the required level of quantification. If a zero-tolerance approach is taken, a change of 1 per cent gas saturation within the seal would require sequestration to stop and the information provided by seismic P-wave velocity suffices. However, if some leakage from the reservoir is tolerated or regulators would be interested to know if a leak occurs how big this is, and how it evolves over time and space, then CSEM is required. Independent of the regulations, which may vary worldwide and with time, it is clear that quantifying a leak into shallower depths or up to the seabed is important.

Geology and porous media are complex, and given the non-uniqueness of the deterministic inversion, using complementary geophysical data sets is vital. Park et al. (2017) and Gasperikova et al. (2022) discuss the merits of integrating CSEM with seismic and gravity data for post-injection monitoring of CCS reservoirs.

Dean & Tucker (2017)'s risk-based framework for measurement, monitoring, and verification (MMV) of the Golden-eye storage complex in the UK, at similar water depth (120 m) and in close proximity to Scanner, concludes that CSEM is not a recommended method as the contrast expected in electric resistivity would not be detectable and notes issues with CSEM in shallow water. There are no CSEM models or data presented in their publication to justify this conclusion. Similarly, unsupported by data analysis, the 2015 IEAGHG report (IEAGHG 2015) infers that CSEM does not enhance MMV strategies. Our suite of synthetic modelling demonstrates unequivocally that the CSEM method adds value in monitoring CCS sites.

Our inversion models consider several scenarios, indicating that a leak via a chimney of homogeneous and varying CO_2 saturations can be imaged by CSEM (Figures 11, 12, 14 and 8). We demonstrate that monitoring CO_2 leakage scenarios through a chimney 500 m wide and fully connected to the reservoir, using marine CSEM, is achievable and aided by: a) adding a vertical E-field component, b) inverting multiple frequencies, c) applying seismic constraints to the injection reservoir, d) employing an ultra-fine (few meters) starting mesh (adaptive refined), and e) site-specific inversion parameterisation.

We note that fluid saturations can be underestimated if the subsurface clay content is unaccounted for when using Archie's law for clean sands. Therefore, Archie's equation requires modification for rock physics property analysis or inversion modelling of a CCS site (Juhasz 1981). Realistic rock physics and dynamic modelling (Commer et al. 2022) are key in assessing the feasibility and interpreting geophysical data with the purpose of CCS monitoring. A change in porosity of 10 per cent in the chimney, composed of clay and silt fully saturated with brine, extending from 200 to 1000 mbsf, is detectable as a conductive anomaly in both E_y and E_z electric field components when inverting multiple frequencies consisting of the 1 Hz fundamental frequency and the odd harmonics up to 11 Hz. Alterations in chimney porosity may imply increased permeability, which manifests as variations in electrical resistivity, detectable by constrained CSEM modelling (Figure 12 and Figure 14).

A marine CSEM study by Attias et al. (2016) delineated a similar chimney structure (saturated with gas hydrate) using seismically-constrained 2D CSEM inversion of the E_y component. In comparison, our unconstrained 2D CSEM inversion of the E_z component for a chimney containing homogeneous S_{CO_2} of 20 per cent and 50 per cent produced satisfactory lateral resolution (Figures 11 and 12). However, inversion of a chimney saturated homogeneously by CO_2 less than 20 per cent requires seismic constraints to resolve the true model (Figure 11b-c). In the synthetic models discussed above, E_z is more sensitive to alterations in the chimney's S_{CO_2} than E_y. E_z inversion provides a more satisfactory lateral resolution to CO_2 saturated chimney. Combined E_z and E_y inversions predict the true resistivity model better.

We assume CO_2 vertical upward migration via the chimney at a rate of 0.1 m/day (Marín-Moreno et al. 2019), which has been used to determine the saturation distribution of a leak via the chimney after 5 and 25 years of injection. According to the modelling presented in Figure 14, a leak after 5 years of injection and for the specific boundary conditions and geology modelled could be detected. This observation could have implications as to how early CSEM monitoring should start and also highlights the importance of making this decision in conjunction with predictions from an area-specific flow model. In accordance with Marín-Moreno et al. (2019) the CO_2 migrates 365 m vertically through the modelled chimney ($\sim$ 600 m length) in 10 years. This implies that, in case of a CO_2 leak, CSEM monitoring needs to be conducted before 10 years of injection, as recommended for cases where no chimney is present (Fawad & Mondol 2021).

5.1   Study limitations

Our study simulates and analyses CO_2 leaking through a fluid pathway in the seal above a CCS reservoir with a specific geometry and specific rock physics parameters (Table 1, Figure 3 and Figure 4). The models are a proxy for an existing fluid escape feature in the North Sea (Scanner Pockmark). However, the North Sea has many fluid pathways with similar characteristics (Karstens & Berndt 2015) so our work provides a basis for studying such fluid escape features. Our modelling is based on a realistic and relevant geological worst-case leakage scenario in an area where CCS projects are considered. The synthetic models were constructed using realistic survey geometry; however, perturbation analysis to asses navigational uncertainties was not performed. Porosity and temperature affect resistivity. Generally, porosity decreases with depth due to compaction of the sediment above, which may increase the resistivity (Athy 1930a), and temperature increases with depth due to the geothermal gradient, which may cause the pore water to warm and decrease resistivity (Arps 1953). Depending on the rock matrix and the pore fluid filling the pore space, these two effects may counteract each

other. Therefore, adequate modelling of deeper reservoirs and seal formations requires consideration of porosity and temperature effects on the formation's resistivity. In addition, studies on geophysical monitoring of CCS can benefit from appropriate and project-specific dynamic modelling, since generalisations are not always valid (Gasperikova et al. 2022).

Our deterministic inversion results have the uncertainties of a smooth regularised inversion. Quantifying uncertainties on a deterministic CSEM inversion is not typically addressed and sensitivity analyses alone are not enough to equate to the resolution of modelled features. There are three approaches in recent work to estimate CSEM uncertainties: 1) Through fully nonlinear and Bayesian approach (Ray 2021) 2) smooth optimization-based stochastic posterior approximation (Blatter et al. 2022) and 3) using 3D seismic and geology knowledge (scenario base inversion) as constraints to determine uncertainties with statistical inversion techniques (Causse 2023). Ideally, depending on the project risk profile and computer power available, one or more of these approaches could be used in future work. Our study does not model CSEM survey repeatability as we do not consider it relevant when looking at resistivity inversions. Orange et al. (2009), Andréis & MacGregor (2011) and Tietze et al. (2019) discussed the limitations of survey repeatability (raw data-driven analysis) to monitor CCS sites. However, Shantsev et al. (2020) demonstrates that the limitations associated with marine CSEM navigation repeatability are insignificant when CSEM data is processed rigorously and coupled with a well-parameterized inversion scheme.

We acknowledge the limitations of a 2D analysis to describe a pipe-like structure that is a 3D feature; however, a 3D analysis requires substantial computing resources. and it is beyond the scope of this paper.

6 CONCLUSIONS

This study analyses the capability of the marine CSEM technique to detect leakage from a CO_2 storage site through vertical fluid conduits above the reservoir. For this purpose, we generated a suite of unconstrained and constrained synthetic CSEM inversion models and we infer the following:

(1) CSEM inverse modelling detects gas leakage through a chimney. We have demonstrated that CSEM is sensitive to a 10 per cent porosity increase within a 500 m wide chimney (Figure 9) and variations in CO_2 saturation within the chimney (Figure 9, Figure 8 and Figure A2 in Appendix D). The resistivity contrast due to the modelled porosity increase is moderate (0.2-0.3 Ωm; 10-20 percentage difference). However, for surveys and data sets with navigation errors or noise larger than assumed here, the signal of a similar conductive chimney may not be detected. Our modelling shows that CO_2

saturation differences with more than 20 per cent amplitude percentage differences are likely to be detected.

(2) The vertical component of the electric field has higher sensitivity to changes in the chimney's electrical resistivity than the inline horizontal component, as a result of the modelled vertical chimney geometry. Thus, it is essential to employ both E-field components to optimize carbon storage sites monitoring using marine CSEM to gain higher sensitivity to vertical leakage pathways saturated with CO_2.

(3) At 1 Hz fundamental frequency, receivers at distances greater than 1000 m from the target chimney are more sensitive to the chimney's electrical resistivity than those at closer ranges. However, as frequency increases, nearby receivers gradually become more sensitive. Thus, performing pre-survey CSEM synthetic studies can help to determine the ideal receiver positions for mapping regions of interest that are vertically structured.

(4) For upward migration velocities of 0.1m/day through the modelled chimney, monitoring with CSEM should start as early as 5 years after injection.

(5) An integrated approach that combines CSEM and seismic data will help to constrain better the full range of possible saturations (0-100 per cent). Thus, time-lapse CSEM surveys can potentially enhance the current CCS measurement, monitoring, and validation (MMV) strategy, by identifying significant leaks that seismic data alone could not identify. Reducing carbon emissions by 85-95 per cent until 2050 to meet UNFCCC Paris Agreement (2015) requires regulatory monitoring of global CCS operations. Based on the above, we conclude that time-lapse marine CSEM can enhance CO_2 monitoring capabilities.

7 DATA AVAILABILITY

The inversion and modelling package MARE2DEM is open source and can be obtained from the official MARE2DEM website https://mare2dem.bitbucket.io/master/download.html. Model files to recreate the synthetic data may be obtained on reasonable request from the first author.

ACKNOWLEDGMENTS

REFERENCES

Alemu, B. L., Aker, E., Soldal, M., Johnsen, N., & Aagaard, P., 2013. Effect of sub-core scale heterogeneities on acoustic and electrical properties of a reservoir rock: a CO_2 flooding experiment of brine saturated sandstone in a computed tomography scanner, *Geophysical Prospecting*, **61**(1), 235–250.

Andréis, D. & MacGregor, L., 2011. Using csem to monitor production from a complex 3d gas reservoir—a synthetic case study, *The Leading Edge*, **30**(9), 1070–1079.

Archie, G., 1942. The Electrical Resistivity Log as an Aid in Determining Some Reservoir Characteristics, *Transactions of the AIME*, **146**(01), 54–62.

Arps, J. J., 1953. The Effect of Temperature on the Density and Electrical Resistivity of Sodium Chloride Solutions, *Journal of Petroleum Technology*, **5**(10), 17–20.

Athy, L. F., 1930a. Density, porosity, and compaction of sedimentary rocks, *AAPG Bulletin*, **14**, 1–24.

Attias, E., Weitemeyer, K., Minshull, T., Best, A., Sinha, M., Jegen-Kulcsar, M., Hölz, S., & Berndt, C., 2016. Controlled-source electromagnetic and seismic delineation of sub-seafloor fluid flow structures in a gas hydrate province, offshore Norway, *Geophysical Journal International*, **206**, ggw188.

Attias, E., Thomas, D., Sherman, D., Ismail, K., & Constable, S., 2020. Marine electrical imaging reveals novel freshwater transport mechanism in Hawai'i, *Sci. Adv.*, **6**(48), eabd4866.

Audigane, P., Gaus, I., Czernichowski-Lauriol, I., Pruess, K., & Xu, T., 2007. Two-dimensional reactive transport modeling of CO_2 injection in a saline Aquifer at the Sleipner site, North Sea, *American Journal of Science*, **307**.

Bachu, S., 2000. Sequestration of CO_2 in geological media: criteria and approach for site selection in response to climate change, *Energy Conversion and Management*, **41**(9), 953–970.

Baklid, A., Korbol, R., & Owren, G., 1996. Sleipner Vest CO_2 Disposal, CO_2 Injection Into A Shallow Underground Aquifer, in *SPE Annual Technical Conference and Exhibition*, vol. All Days, SPE-36600-MS.

Blatter, D., Morzfeld, M., Key, K., & Constable, S., 2022. Uncertainty quantification for regularized inversion of electromagnetic geophysical data—part i: motivation and theory, *Geophysical Journal International*, **231**(2), 1057–1074.

Brannon, H.R., J. & Osoba, J., 1956. Spectral gamma-ray logging, *Transactions of the AIME*, **207**(01), 30–35.

Bretaudeau, F., Dubois, F., Bissavetsy Kassa, S.-G., Coppo, N., Wawrzyniak, P., & Darnet, M., 2021. Time-lapse resistivity imaging: Csem-data 3-d double-difference inversion and application to the reykjanes geothermal field, *Geophysical Journal International*, **226**(3), 1764–1782.

Brie, A., Pampuri, F., Marsala, A. F., & Meazza, O., 1995. Shear sonic interpretation in gas-bearing sands, *Software - Practice and Experience*, pp. 701–710.

Bull, J., Berndt, C., Minshull, T., Henstock, T. J., Bayrakci, G., Gehrmann, R., Provenzano, G., Böttner, C., Schramm, B., , Callow, B. J., Chapman, M., Birinci, H., Yilo, N., Dewar, M., Baixin, C., Saleem, U., Marin-Moreno, H., Lichtschlag, A., Falcon-Suarez, I., Roche, B., James, R., Connelly, D., Matter, J., Judith, E., KArstens, J., & Angus, B., 2018. Constraining the physical properties of Chimney/pipe structures within sedimentary basins.

Börner, J. H., Wang, F., Weißflog, J., Bär, M., Görz, I., & Spitzer, K., 2015. Multi-method virtual electromagnetic experiments for developing suitable monitoring designs: A fictitious co2 sequestration scenario in northern germany, *Geophysical Prospecting*, **63**(6), 1430–1449.

Böttner, C., Berndt, C., Reinardy, B. T., Geersen, J., Karstens, J., Bull, J. M., Callow, B. J., Lichtschlag, A., Schmidt, M., Elger, J., Schramm, B., & Haeckel, M., 2019. Pockmarks in the Witch Ground Basin, Central North Sea, *Geochemistry, Geophysics, Geosystems*, **20**(4), 1698–1719.

Callow, B., Bull, J. M., Provenzano, G., Böttner, C., Birinci, H., Robinson, A. H., Henstock, T. J., Minshull, T. A., Bayrakci, G., Lichtschlag, A., Roche, B., Yilo, N., Gehrmann, R., Karstens, J., Falcon-Suarez, I. H., & Berndt, C., 2021. Seismic chimney characterisation in the north sea – implications for pockmark formation and shallow gas migration, *Marine and Petroleum Geology*, **133**, 105301.

Callow, B. J., 2021. *Characterising the permeability and structure of fluid-escape conduits in sedimentary basins - application to geological carbon sequestration*, Ph.D. thesis, University of Southampton.

Cartwright, J. & Santamarina, C., 2015. Seismic characteristics of fluid escape pipes in sedimentary basins: Implications for pipe genesis, *Marine and Petroleum Geology*, **65**, 126–140.

Causse, E., 2023. Ensemble scenario-based inversion: A new approach for estimating the uncertainty of resistivity models derived from 3d controlled source electromagnetic data, *Geophysical Prospecting*, **71**(5), 847–875.

Chadwick, R. A., Kirby, G. A., Holloway, S., Gregersen, U., Johannessen, P., Zweigel, P., & Arts, R., 2002. Saline aquifer co2 storage (sacs2). final report: Geological characterisation of the utsira sand reservoir and caprocks (work area 1), Report, British Geological Survey.

Chadwick, R. A., Zweigel, P., Gregersen, U., Kirby, G. A., Holloway, S., & Johannessen, P. N., 2004. Geolog-

ORIGINAL UNEDITED MANUSCRIPT

ical reservoir characterization of a CO_2 storage site: The Utsira Sand, Sleipner, northern North Sea, *Energy*, **29**(9), 1371–1381.

Chadwick, R. A., Arts, R., & Eiken, O., 2005. 4D seismic quantification of a growing CO¡sub¿2¡/sub¿ plume at Sleipner, North Sea, *Geological Society, London, Petroleum Geology Conference series*, **6**(1), 1385–1399.

Chadwick, R. A., Marchant, B. P., & Williams, G. A., 2014. CO_2 storage monitoring: leakage detection and measurement in subsurface volumes from 3D seismic data at Sleipner, *Energy Procedia*, **63**, 4224–4239.

Chadwick, R. A., Williams, G. A., & Falcon-Suarez, I., 2019. Forensic mapping of seismic velocity heterogeneity in a CO_2 layer at the Sleipner CO_2 storage operation, North Sea, using time-lapse seismics, *International Journal of Greenhouse Gas Control*, **90**, 19.

Collett, T. S. & Ladd, J. W., 2000. (Table 4) Volume of natural gas within the downhole log-inferred gas-hydrate occurrences in ODP Leg 164 sites, PANGAEA, In supplement to: Collett, TS; Ladd, JW (2000): Detection of gas hydrate with downhole logs and assessment of gas hydrate concentrations (saturations) and gas volumes on the Blake Ridge with electrical resistivity log data. In: Paull, CK; Matsumoto, R; Wallace, PJ; Dillon, WP (eds.) Proceedings of the Ocean Drilling Program, Scientific Results, College Station, TX (Ocean Drilling Program), 164, 1-13, https://doi.org/10.2973/odp.proc.sr.164.219.2000.

Commer, M., Gasperikova, E., & Doughty, C., 2022. Improved geophysical monitoring of carbon sequestration through parameter linkage to reservoir modeling, *International Journal of Greenhouse Gas Control*, **119**, 103717.

Constable, S., 2010. Ten years of marine CSEM for hydrocarbon exploration, *Geophysics*, **75**(5), 75A67–75A81.

Copestake, P., Sims, A., Crittenden, S., Hamar, G., Ineson, J., Rose, P., & Tringham, M., 2003. *The Millennium Atlas: petroleum geology of the central and northern North Sea.*, book section Lower Cretaceous, pp. 191–211, The Geological Society of London.

Davies, R. J., 2003. Kilometer-scale fluidization structures formed during early burial of a deep-water slope channel on the Niger Delta, *Geology*, **31**(11), 949–952.

Dean, M. & Tucker, O., 2017. A risk-based framework for measurement, monitoring and verification (mmv) of the goldeneye storage complex for the peterhead ccs project, uk, *International Journal of Greenhouse Gas Control*, **61**, 1–15.

Domenico, S. N., 1976. Effect of brine-gas mixture on velocity in an unconsolidated sand reservoir, *Geophysics*, **41**(5), 882–894.

Dupuy, B., Romdhane, A., Nordmann, P.-L., Eliasson, P., & Park, J., 2021. Bayesian rock physics inversion: application to co2 storage monitoring, *GEOPHYSICS*, pp. 1–73.

Falcon-Suarez, I., Papageorgiou, G., Chadwick, R. A., North, L., Best, A. I., & Chapman, M., 2018. CO_2-brine flow-through on an Utsira Sand core sample: Experimental and modelling. Implications for the Sleipner storage field, *International Journal of Greenhouse Gas Control*, **68**, 236–246.

Falcon-Suarez, I., Lichtschlag, A., Marin-Moreno, H., Giorgos, P., Sahoo, S. K., Roche, B., Callow, B., Gehrmann, R. A., Chapman, M., & North, L., 2021. Core-scale geophysical and hydromechanical analy-

sis of seabed sediments affected by CO_2 venting, *International Journal of Greenhouse Gas Control*.

Fawad, M. & Mondol, N. H., 2021. Monitoring geological storage of CO_2: a new approach, *Scientific Reports*, **11**(1), 5942.

Furre, A.-K., Meneguolo, R., Ringrose, P., & Kassold, S., 2019. Building confidence in CCS: From Sleipner to the Northern Lights Project, *First Break*, **37**(7), 81–87.

Gafeira, J. & Long, D., 2015. *Geological investigation of pockmarks in the Braemar Pockmarks SCI*, JNCC UK.

Gasperikova, E., Appriou, D., Bonneville, A., Feng, Z., Huang, L., Gao, K., Yang, X., & Daley, T., 2022. Sensitivity of geophysical techniques for monitoring secondary co2 storage plumes, *International Journal of Greenhouse Gas Control*, **114**, 103585.

Gehrmann, R., Romdhane, M. A., Park, J., & Eliasson, P., 2021a. CSEM for CO2 Storage–Feasibility Study at Smeaheia to Optimise Acquisition, in *TCCS–11. CO2 Capture, Transport and Storage. Trondheim 22nd–23rd June 2021. Short Papers from the 11th International Trondheim CCS Conference*.

Gehrmann, R. A., Provenzano, G., Böttner, C., Marín-Moreno, H., Bayrakci, G., Tan, Y. Y., Yilo, N. K., Djanni, A. T., Weitemeyer, K. A., Minshull, T. A., Bull, J. M., Karstens, J., & Berndt, C., 2021b. Porosity and free gas estimates from controlled source electromagnetic data at the scanner pockmark in the north sea, *International Journal of Greenhouse Gas Control*, **109**, 103343.

Girard, J. F., Coppo, N., Rohmer, J., Bourgeois, B., Naudet, V., & Schmidt-Hattenberger, C., 2011. Time-lapse CSEM monitoring of the Ketzin (Germany) CO_2 injection using 2×MAM configuration, *Energy Procedia*, **4**, 3322–3329.

Goldberg, D., Takahashi, T., & Slagle, A., 2008. Carbon dioxide sequestration in deep-sea basalt, *Proceedings of the National Academy of Sciences of the United States of America*, **105**, 9920–5.

Goswami, B. K., Weitemeyer, K. A., Minshull, T. A., Sinha, M. C., Westbrook, G. K., & Marín-Moreno, H., 2016. Resistivity image beneath an area of active methane seeps in the west Svalbard continental slope, *Geophysical Journal International*, **207**(2), 1286–1302.

Hansen, H., Eiken, O., & Aasum, T. O., 2005. The path of a carbon dioxide molecule from a gas-condensate reservoir, through the amine plant and back down into the subsurface for storage. Case study: The Sleipner area, South Viking Graben, Norwegian North Sea, in *SPE Offshore Europe Oil and Gas Exhibition and Conference*, vol. All Days, SPE-96742-MS.

Harper, M. L., 1971. Approximate Geothermal Gradients in the North Sea Basin, *Nature*, **230**(5291), 235–236.

Hoteit, H., Fahs, M., & Soltanian, M. R., 2019. Assessment of CO_2 Injectivity During Sequestration in Depleted Gas Reservoirs, *Geosciences (Switzerland)*, **9**, 199.

IEA, 2021. Net zero by 2050, Paris, Project report, IEA.

IEAGHG, 2015. Review of offshore monitoring for CCS projects, Project report, IEAGHG.

Judd, A., Long, D., & Sankey, M., 1994. Pockmark formation and activity, U.K. Block 15/25, North Sea. Bull Geol Soc Denmark, *Bulletin of the Geological Survey of Denmark*, **41**, 34–49.

Juhasz, I., 1981. Normalised Qv - The Key To Shaly Sand Evaluation Using The Waxman-Smits Equation In

The Absence Of Core Data, in *SPWLA 22nd Annual Logging Symposium*, vol. All Days, SPWLA-1981-Z.

Karstens, J. & Berndt, C., 2015. Seismic chimneys in the Southern Viking Graben – Implications for palaeo fluid migration and overpressure evolution, *Earth and Planetary Science Letters*, **412**, 88–100.

Key, K., 2009. 1D inversion of multicomponent, multifrequency marine CSEM data: Methodology and synthetic studies for resolving thin resistive layers, *Geophysics*, **74**.

Key, K., 2016. MARE2DEM: a 2-D inversion code for controlled-source electromagnetic and magnetotelluric data, *Geophysical Journal International*, **207**(1), 571–588.

Lee, M., 2004. Elastic velocities of partially gas-saturated unconsolidated sediments, *Marine and Petroleum Geology - MAR PETROL GEOL*, **21**.

Li, J., Roche, B., Bull, J. M., White, P. R., Leighton, T. G., Provenzano, G., Dewar, M., & Henstock, T. J., 2020. Broadband acoustic inversion for gas flux quantification—application to a methane plume at scanner pockmark, central north sea, *Journal of Geophysical Research: Oceans*, **125**(9), e2020JC016360.

MacGregor, L. & Sinha, M., 2000. Use of Marine Controlled Source Electromagnetic Sounding for Sub-Basalt Exploration, *Geophysical Prospecting*, **48**, 1091–1106.

Marín-Moreno, H., Bull, J. M., Matter, J. M., Sanderson, D. J., & Roche, B. J., 2019. Reactive transport modelling insights into CO_2 migration through sub-vertical fluid flow structures, *International Journal of Greenhouse Gas Control*, **86**, 82–92.

Mavko, G., Mukerji, T., & Dvorkin, J., 2009. *The Rock Physics Handbook: Tools for Seismic Analysis of Porous Media*, Cambridge University Press, 2nd edn.

Orange, A., Key, K., & Constable, S., 2009. The feasibility of reservoir monitoring using time-lapse marine csem, *GEOPHYSICS*, **74**(2), F21–F29.

Park, J., Viken, I., Bjørnarå, T., & Aker, E., 2011. CSEM data analysis for Sleipner CO_2 storage, 6th *Trondheim CCS Conference, June 14-16*.

Park, J., Sauvin, G., & Vöge, M., 2017. 2.5D Inversion and Joint Interpretation of CSEM Data at Sleipner CO_2 Storage, *Energy Procedia*, **114**, 3989–3996.

Paul, M. & Jobson, L. M., 1991. Geotechnical properties of soft clays from the Witch Ground Basin, central North Sea, *Geological Society, London, Engineering Geology Special Publications*, **7**(1), 151–156.

Ramirez, A. & Friedmann, J., 2008. Joint reconstruction of CO_2 plumes using disparate data, Technical report, Lawrence Livermore National Lab. (LLNL), Livermore, CA (United States).

Ray, A., 2021. Bayesian inversion using nested trans-dimensional gaussian processes, *Geophysical Journal International*, **226**(1), 302–326.

Riedel, M., Long, P., Liu, C., Schultheiss, P., & Collett, T., 2006. 8. Physical properties of near-surface sediments at southern Hydrate Ridge: results from ODP Leg 204, *Proceedings of the Ocean Drilling Program, Scientific Results. Tréhu, A.M., Bohrmann, G., Torres, M.E., and Colwell, F.S. (Eds.)*, **204**.

Ringrose, P. S. & Meckel, T. A., 2019. Maturing global CO_2 storage resources on offshore continental margins to achieve 2DS emissions reductions, *Scientific Reports*, **9**(1), 17944.

Robinson, A., Callow, B. J., Böttner, C., Yilo, N. K., Provenzano, G., Falcon-Suarez, I. H., Moreno, H. M.,

Lichtschlag, A., Bayrakci, G., Gehrmann, R., Parkes, L., Roche, B., Saleem, U., Schramm, B., Waage, M., Lavayssiere, A., Li, J., Eyvazi, F. J., Sahoo, S., Deusner, C., Kossel, E., Minshull, T., Berndt, C., Bull, J., Dean, M., James, R., Chapman, M., Best, A. I., Bünz, S., Chen, B., Connelly, D., Elger, J., Haeckel, M., Henstock, T., Karstens, J., Macdonald, C., Matter, J., North, L. J., & Reinardy, B., 2021. Multiscale characterisation of chimneys/pipes: fluid escape structures within sedimentary basins, *International Journal of Greenhouse Gas Control*.

Rutqvist, J., Rinaldi, A. P., Cappa, F., Jeanne, P., Mazzoldi, A., Urpi, L., Guglielmi, Y., & Vilarrasa, V., 2016. Fault activation and induced seismicity in geological carbon storage – Lessons learned from recent modeling studies, *Journal of Rock Mechanics and Geotechnical Engineering*, **8**(6), 789–804.

Schmidt-Hattenberger, C., Bergmann, P., Labitzke, T. I. M., SchrÖDer, S., Krüger, K., Rücker, C., & Schütt, H., 2011. Monitoring of geological CO_2 storage with electrical resistivity tomography (ERT): Results from a field experiment near Ketzin/Germany, *Energy Procedia*, **4**, 3363–3370.

Schmidt-Hattenberger, C., Bergmann, P., Labitzke, T., Schröder, S., Krüger, K., Rücker, C., & Schütt, H., 2012. A Modular Geoelectrical Monitoring System as Part of the Surveillance Concept in CO_2 Storage Projects, *Energy Procedia*, **23**, 400–407.

Shantsev, D. V., Nerland, E. A., & Gelius, L.-J., 2020. Time-lapse CSEM: how important is survey repeatability?, *Geophysical Journal International*, **223**(3), 2133–2147.

Shell-UK-limited, 2014. Peterhead CCS Project - Offshore environmental statement, Project report, Shell-UK-limited.

Sinha, M., Patel, P., Unsworth, M., Owen, T., & Maccormack, M., 1990. An active source EM sounding system for marine use, *Marine Geophysical Researches*, **12**, 59–68.

Stoker, M. S., Balson, P. S., Long, D., & Tappin, D. R., 2011. An overview of the lithostratigraphical framework for the Quaternary deposits on the United Kingdom continental shelf, Tech. rep., British Geological Survey, This item has been internally reviewed but not externally peer-reviewed.

Streich, R., Becken, M., & Ritter, O., 2010. Imaging of co2 storage sites, geothermal reservoirs, and gas shales using controlled-source magnetotellurics: Modeling studies, *Geochemistry*, **70**, 63–75.

Tietze, K., Ritter, O., Patzer, C., Veeken, P., & Dillen, M., 2019. Repeatability of land-based controlled-source electromagnetic measurements in industrialized areas and including vertical electric fields, *Geophysical Journal International*, **218**(3), 1552–1571.

Vielstädte, L., Linke, P., Schmidt, M., Sommer, S., Haeckel, M., Braack, M., & Wallmann, K., 2019. Footprint and detectability of a well leaking co2 in the central north sea: Implications from a field experiment and numerical modelling, *International Journal of Greenhouse Gas Control*, **84**, 190–203.

Waxman, M. & Smits, L., 1968. Electrical Conductivities in Oil-Bearing Shaly Sands, *Society of Petroleum Engineers Journal*, pp. 107–122.

Weitemeyer, K. A., Constable, S., & Tréhu, A. M., 2011. A marine electromagnetic survey to detect gas hydrate at Hydrate Ridge, Oregon, *Geophysical Journal International*, **187**(1), 45–62.

Williams, G. A. & Chadwick, R. A., 2021. Influence of reservoir-scale heterogeneities on the growth, evo-

lution and migration of a CO_2 plume at the Sleipner Field, Norwegian North Sea, *International Journal of Greenhouse Gas Control*, **106**, 103260.

Wirianto, M., Mulder, W. A., & Slob, E. C., 2010. A feasibility study of land csem reservoir monitoring in a complex 3-d model, *Geophysical Journal International*, **181**(2), 741–755.

Wyllie, M. & Gregory, A., 1953. Formation Factors of Unconsolidated Porous Media: Influence of Particle Shape and Effect of Cementation, *Journal of Petroleum Technology*, **5**(04), 103–110.

Zweigel, P., Arts, R., Lothe, A., & Lindeberg, E., 2004. Reservoir geology of the utsira formation at the first industrial-scale underground co2 storage site (sleipner area, north sea), *Geological Society, London, Special Publications*, **233**, 165 – 180.
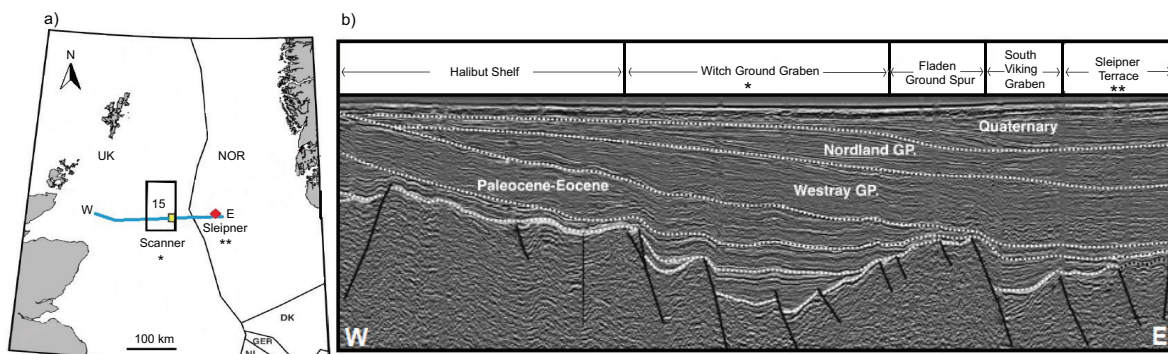
Figure 1. Regional geologic setting and stratigraphy of the Witch Ground Basin in the North Sea. a) The Scanner study area (yellow box inside license block 15/25) is highlighted as well as the Sleipner field (red diamond) and position of the regional seismic line (blue line) shown in b) modified from Callow (2021). b) A regional seismic cross-section, trending west to east across the Central North Sea and the Witch Ground Graben, after Callow (2021) and Copestake et al. (2003). Six stratigraphic intervals are highlighted. The Scanner pockmark area is in the seismic section under the 'Witch Ground Graben' (one star) while Sleipner is under the 'Sleipner Terrace' label (two stars).
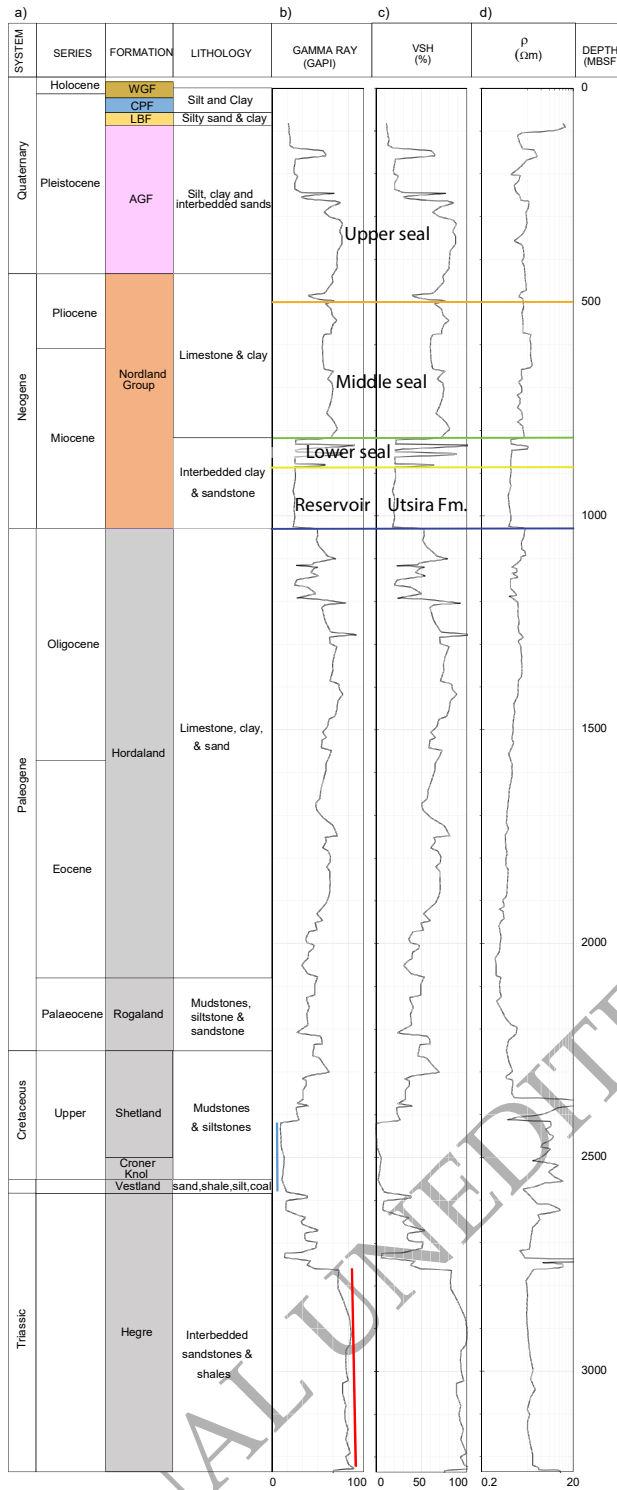
Figure 2. a) Regional chronostratigraphy of the model area, the Witch Ground Basin and Sleipner Terrace in the North Sea, as discussed in section 2. WGF stands for Witch Ground Formation, CPF for Coal Pit Formation and AGF for Aberdeen Ground Formation. Well-logs for 15/9-13 (Sleipner) from Park et al. (2017). a) Measured gamma-ray intensity, the blue line centred at 2500 m depth marks the GR_{min} and the red line centrer at 3000 m depth marks the GR_{max} used to calculate the volume of shale or clay (V_{SH}). b) Calculated V_{SH} from GR and c) resistivity log. The three seal intervals as described in section 2 are indicated in b), c) and d); the orange line corresponds to the base of the upper seal, the green line is the base of the middle seal and the yellow line is the base of the lower seal. The base of the Utsira reservoir is indicated with a navy blue line.
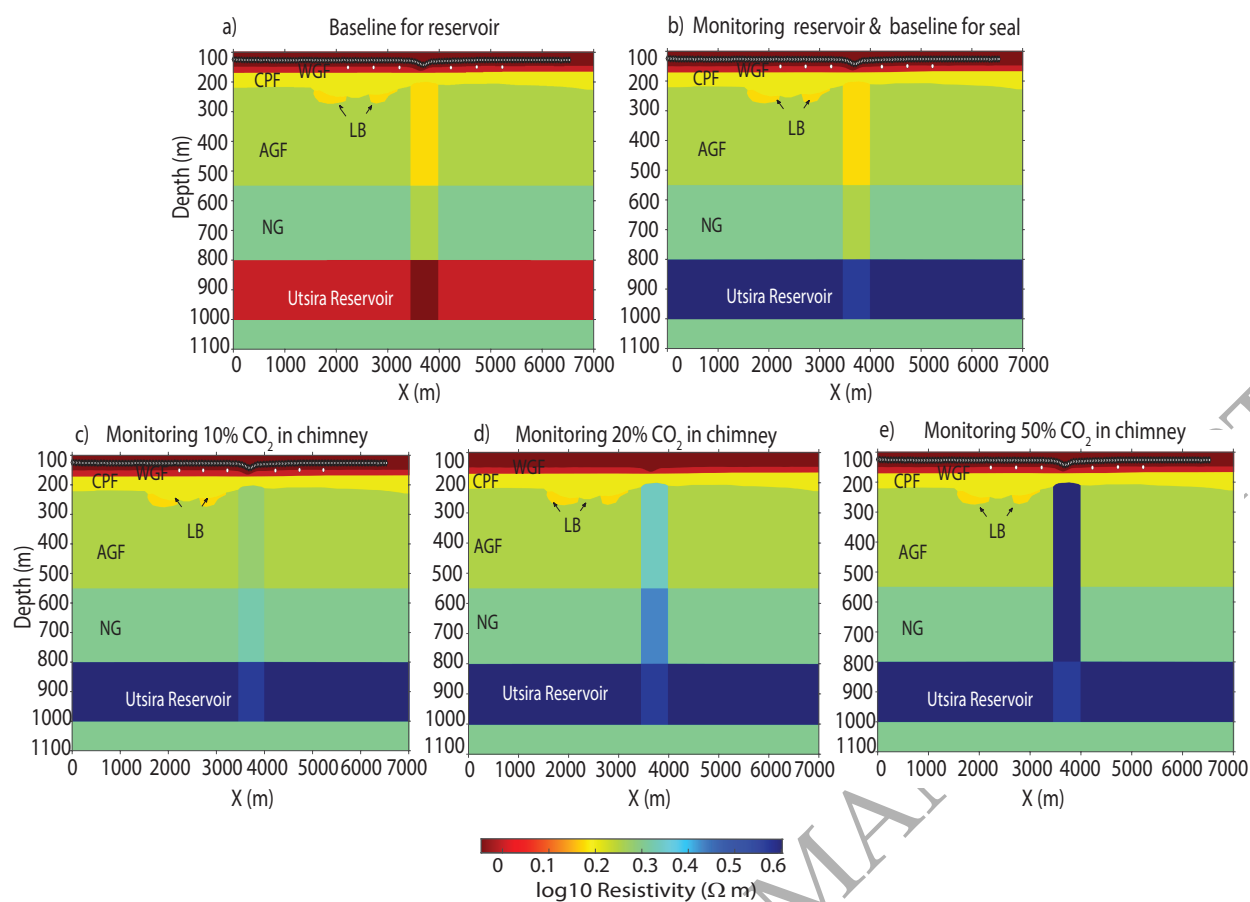
Figure 3. True 2D resistivity model scenarios considered to analyse the detectability of a CO_2 leak through a chimney. The Utsira Reservoir is a saline aquifer and we model it without CO_2 in a) and with injected CO_2 reaching 50 per cent CO_2 saturation within the reservoir in b) to e). We model scenarios b) without CO_2 escaping into the chimney, c) CO_2 saturating the chimney by 10 per cent, d) 20 per cent, and e) 50 per cent. The baseline models (a,b) contain a chimney (or fractures) with a porosity that is 10 per cent higher than the surrounding sediments. The baseline models serve as the reference points to analyse CO_2 changes within the reservoir and the seal. As we model CO_2 leaking through the chimney we focus on the second baseline model b). No leakage has occurred through the chimney ($S_{CO2} = 0$) in model b). The models after leakage through the chimney in c) are the same as b) but with $S_{CO2} = 10$ per cent within the chimney; d) same as b with $S_{CO2} = 20$ per cent within the chimney and e) same as b with $S_{CO2} = 50$ per cent within the chimney. The porosity and resistivity values for each formation, indicated in this figure can be found in Tables 1 and 2.
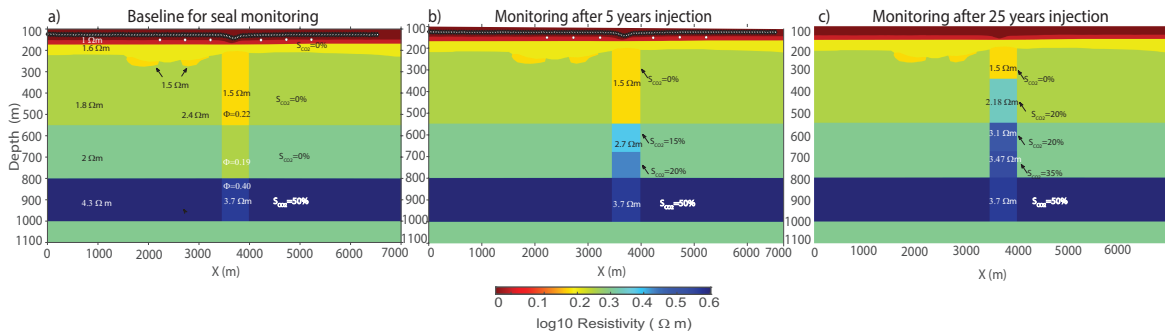
Figure 4. True 2D resistivity model scenarios considering the detectability of a CO_2 leak through a chimney with variable saturations representing different times after CO_2 injection has started, as per dynamic modeling from Marín-Moreno et al. (2019). On the left column are the true resistivity models. a) True model after injection, including 50 per cent CO_2 saturation within the Utsira formation (saline aquifer). No leakage has occurred through the chimney (S_{CO2} =0). b) True model with leakage through the chimney after 5 years of CO_2 injection and c) True model with leakage through the chimney after 25 years of CO_2 injection.
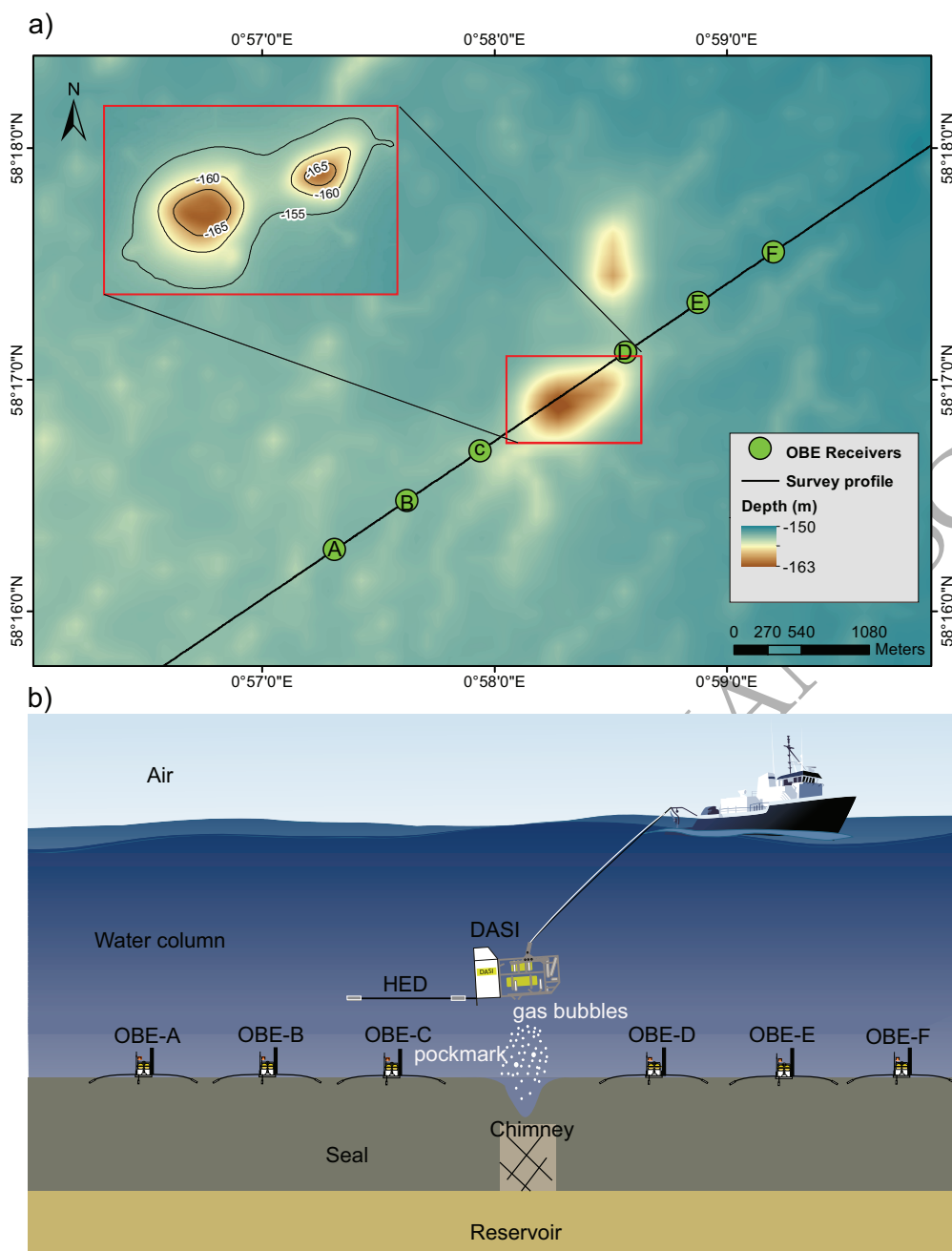
Figure 5. a) Survey layout on a 10 m bathymetry grid from Bull et al. (2018) of the Scanner pockmark (red square). On the top left, a more detailed (2.5 m) bathymetry map of the Scanner pockmark (red square) in a). b) Schematic of the CSEM method (not drawn to scale): the deep-towed active source instrument, DASI (Sinha et al. 1990) is towed across the Scanner pockmark (black line in a) with six OBE receivers spaced 500 m apart and deployed on either side of the pockmark and associated seismic chimney. Sketch in b) modified from Weitemeyer et al. (2011)
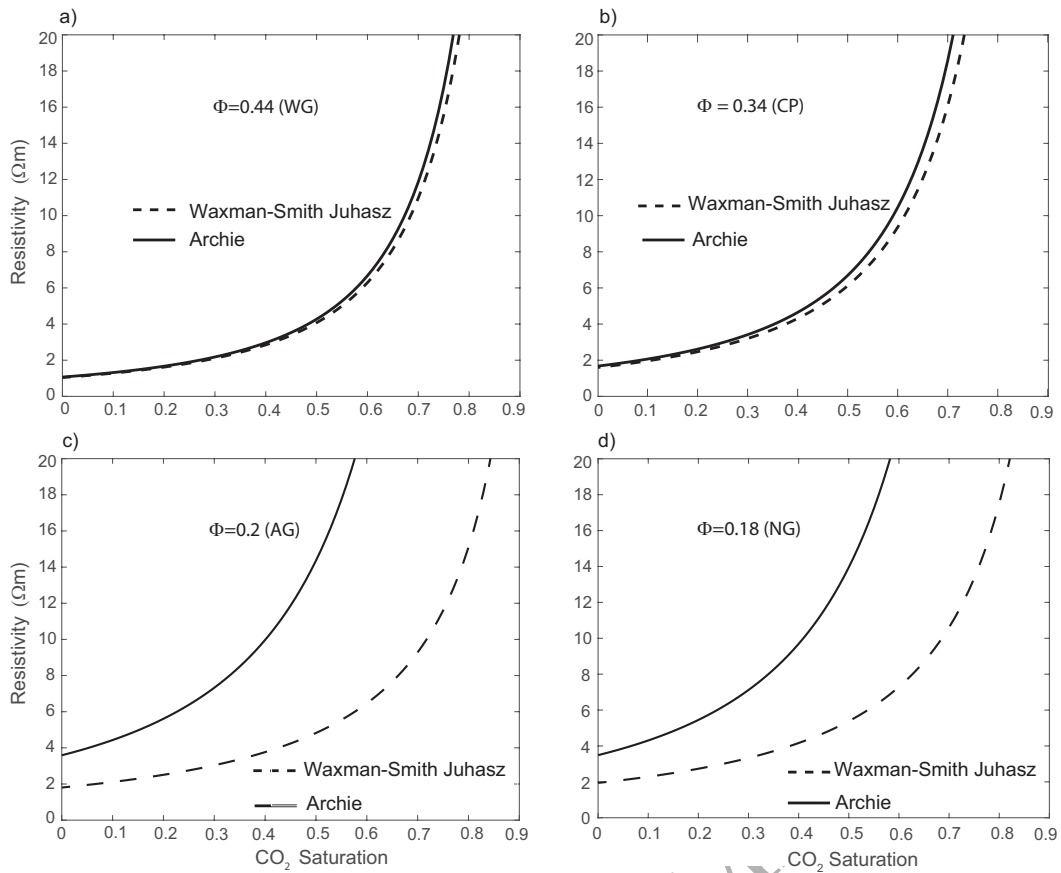
Figure 6. Resistivity versus CO_2 saturation for modelled seal geological units, all which are clay-rich (a) the Witch Ground formation (WG), (b) the Coal Pit formation (CP), (c) the clay rich Aberdeen Ground formation (AG) and (d) Nordland Group (NG). Archie's saturation versus electrical resistivity relationship (solid line) is compared with the Waxman-Smidt-Juhasz relationship (dashed line). Both relationships are computed for each geological unit with the porosities, ϕ, reported in the literature as per Table 1.
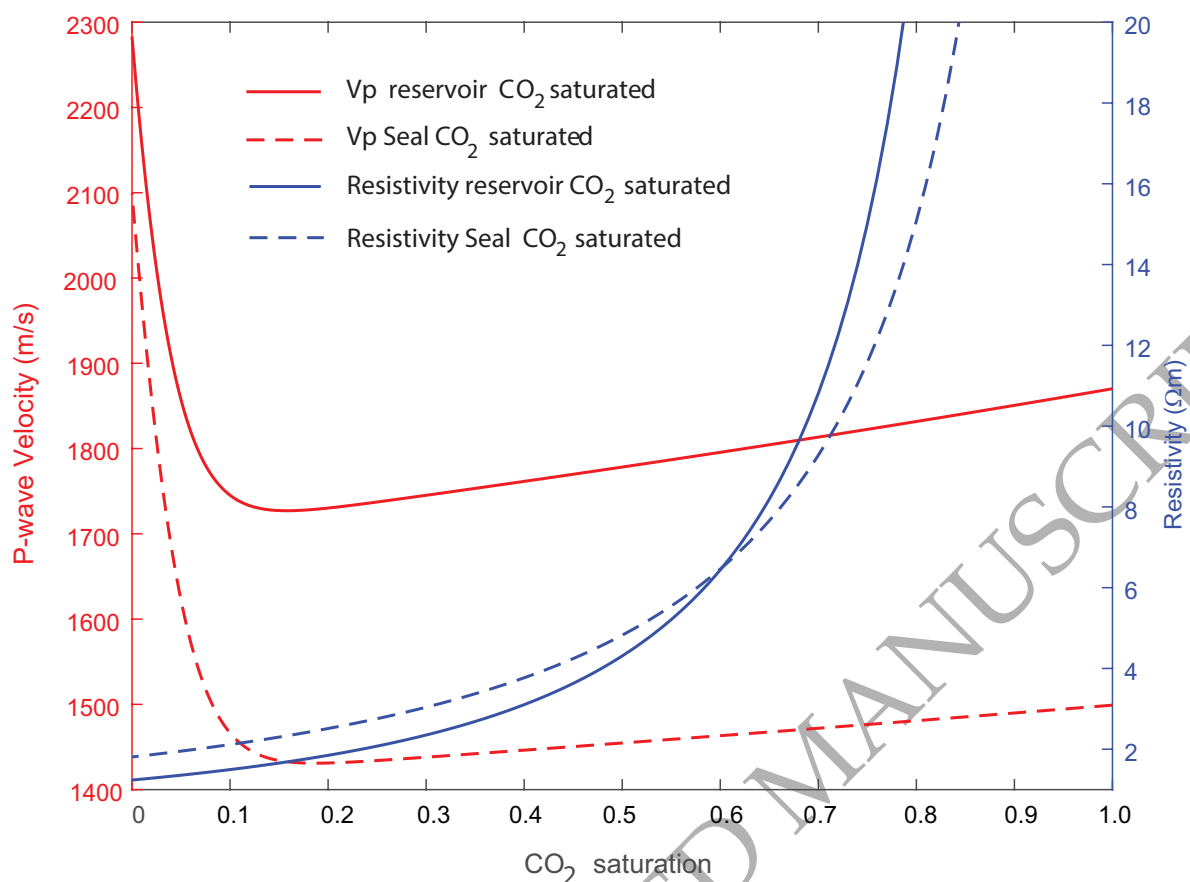
Figure 7. Calculated resistivity for the seal using Juhasz (1981) (dashed blue line) and the reservoir using Archie (1942) (solid blue line) against CO_2 saturation. Resistivity and velocity were calculated for the reservoir (Utsira formation) and seal (from the Witch Ground formation to the Nordland group), using rock physics parameters from our model area in the North Sea, see Table 1. P-wave velocities for the seal (red dashed line) and the reservoir (red solid line) versus CO_2 saturation calculated using a patchy gas saturation distribution (Lee 2004). We use a confining pressure of 2.6 Mpa for the seal and 18.2 Mpa for the reservoir and Brie et al. (1995)'s calibration constant e=30, which provides a nearly uniform gas distribution, inline with experimental results from Lee (2004) for marine unconsolidated sediments.
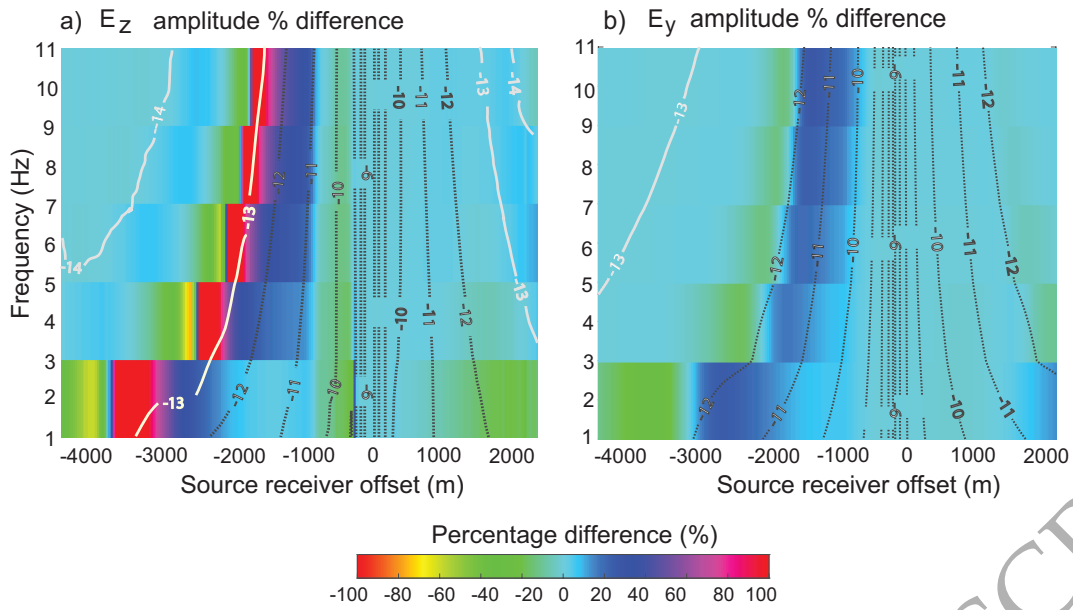
Figure 8. Amplitude percentage difference between chimney saturated with 20 per cent CO_2 (model in Figure 3d) and a chimney saturated with brine or S_{CO_2}=0 (model in Figure 3b) for E_z a) and E_y b). This amplitude anomaly in percentage difference for the 2D model with S_{CO_2}=20 per cent is calculated for a receiver 1000 m away from the chimney (OBE-D). Dashed black contours correspond to the $\log_{10}$ electric field amplitude of the model saturated with 20 per cent CO_2. STEMM-CCS survey instrument noise floor at 10^{-13} V/Am^2, contours below noise floor marked with a continuous white line. Color represents the percentage difference.
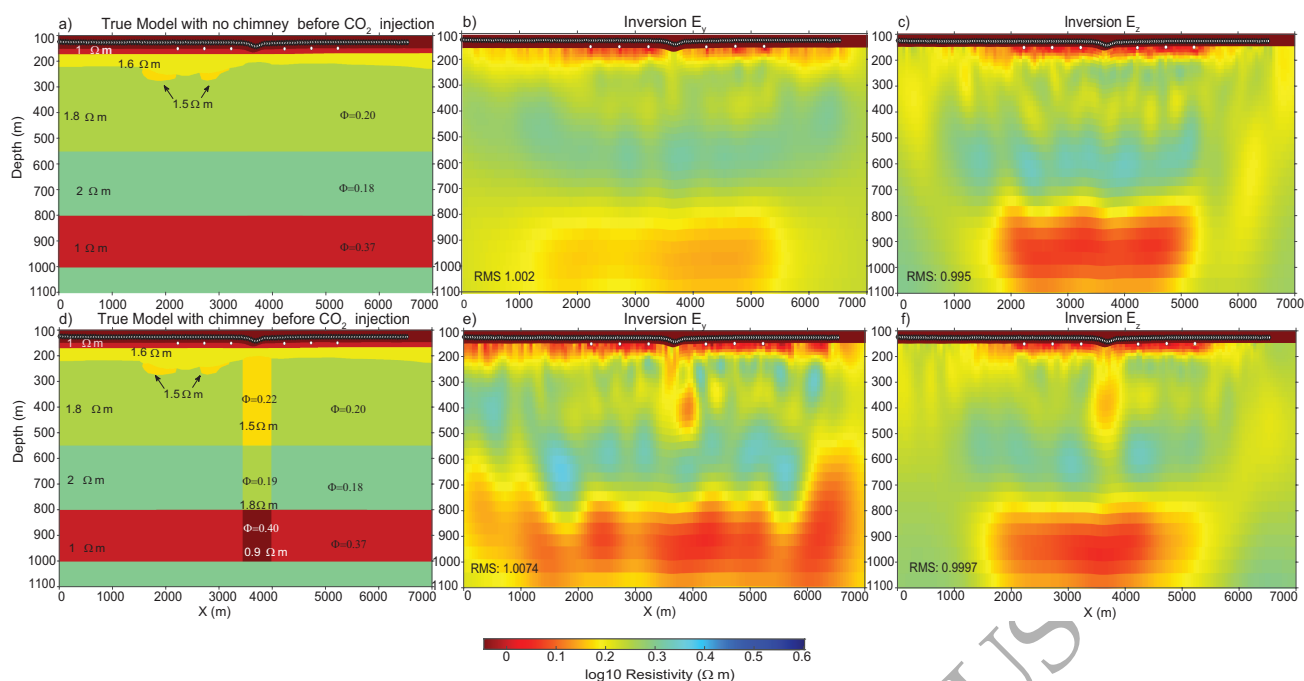
Figure 9. 2D Synthetic resistivity model and resistivity inversion results for the host sediments and for a brine chimney within the host sediments utilizing the geometry, data range, and properties of STEMM-CCS survey line 2. a) True model with no chimney. b) Inversion model of the synthetic data with no chimney for E_y and c) E_z. d) True model with chimney representing a 10 per cent porosity increase and e) inversion model with chimney for E_y and f) E_z. The white circles in the sections represent OBE sites and the white triangles are the transmitter positions. The reservoir layer in these models is 100 per cent saturated with brine (saline aquifer) and, hence a conductive target for CSEM. We use the same colour bar for all our resistivity inversion figures, following the academic convention of hot colours for conductive anomalies and cold colours for the resistive anomalies.
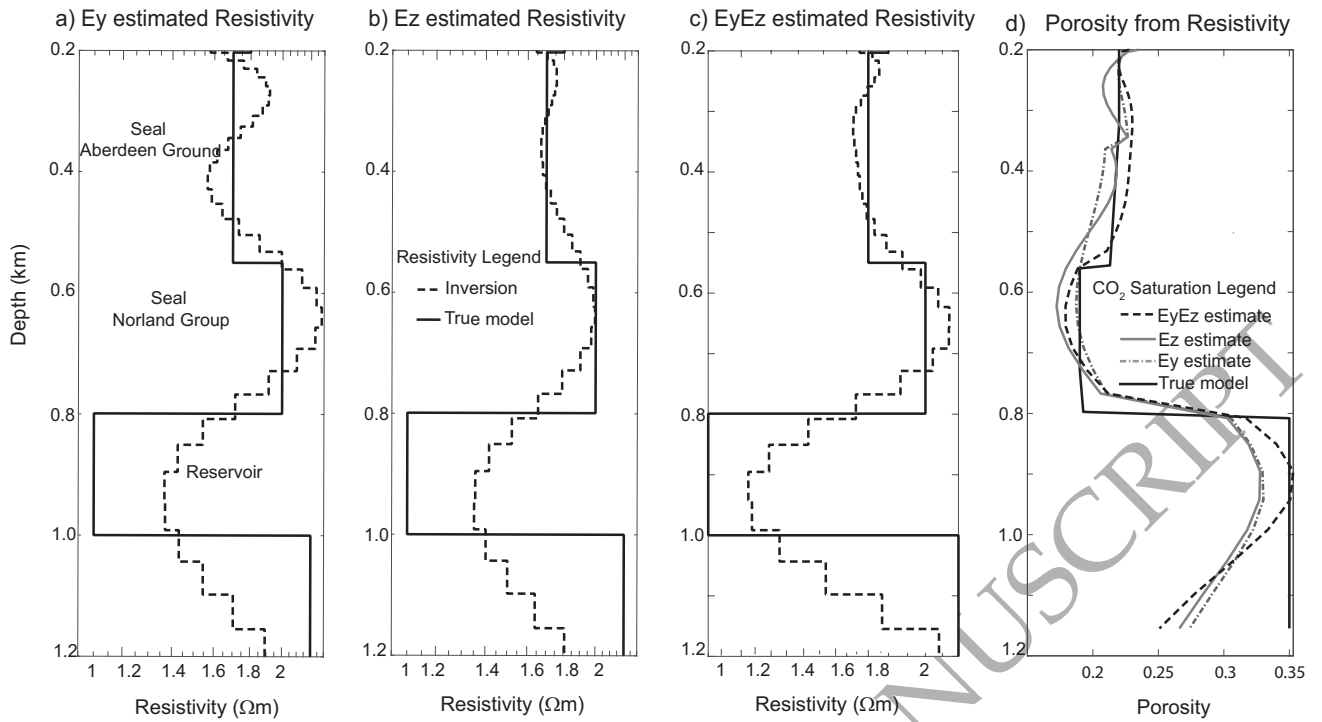
Figure 10. Resistivity and porosity profiles at the chimney (2D model distance = 3.8 km). Resistivity true model (solid line) and inverted (dashed line) resistivity derived from E_y a) E_z b) and E_y E_z c) at the chimney with 10 per cent porosity increase. d) Porosity estimated from E_y (black dotted line), E_z (gray solid line) and joint $E_y E_z$ (black dashed line) while the true model porosity is the (solid black line) using the rock physics model of Waxman-Smits-Juhasz for the clay-rich formation and Archie for the reservoir (Section 3.1).
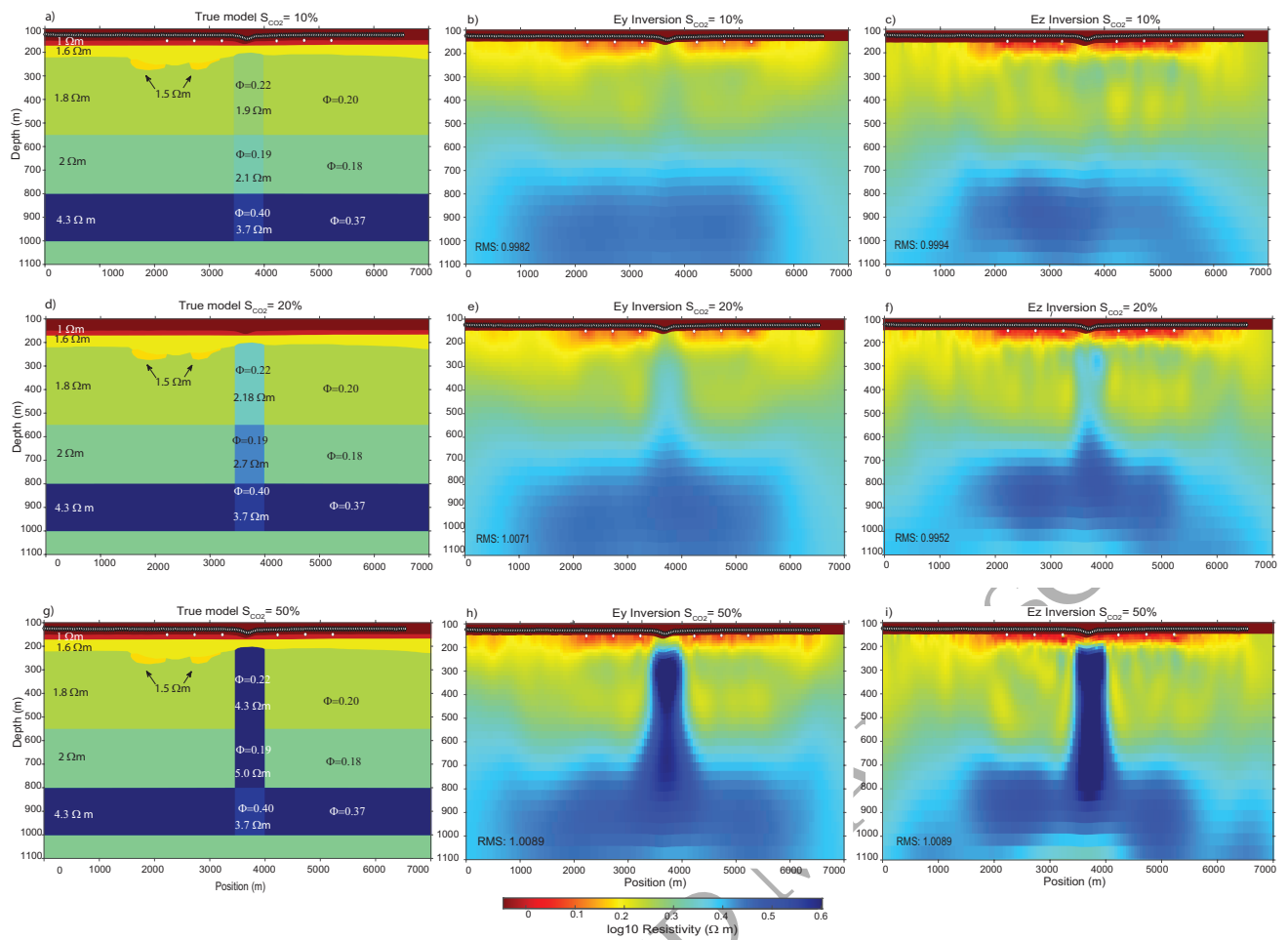
Figure 11. Synthetic (true) models and inversion results for three different scenarios of CO_2 leakage from the reservoir into the chimney, using the geometry, data range, and properties of STEM-CCS survey line 2. In the left column, the true models are shown. a) True model with the chimney saturated with 10 per cent CO_2, d) True model with the chimney saturated with 20 per cent CO_2 and g) True model with the chimney saturated with 50 per cent CO_2. In the second column are the inverted resistivity sections using only E_y data for b) 10 per cent CO_2, e) 20 per cent CO_2, and h) 50 per cent CO_2. In the third column the inverted resistivity sections using only E_z data are shown for c)10 per cent CO_2, f)20 per cent CO_2, and i) 50 per cent CO_2. The circles on inverted models represent OBE sites while the white triangles are the transmitter positions.
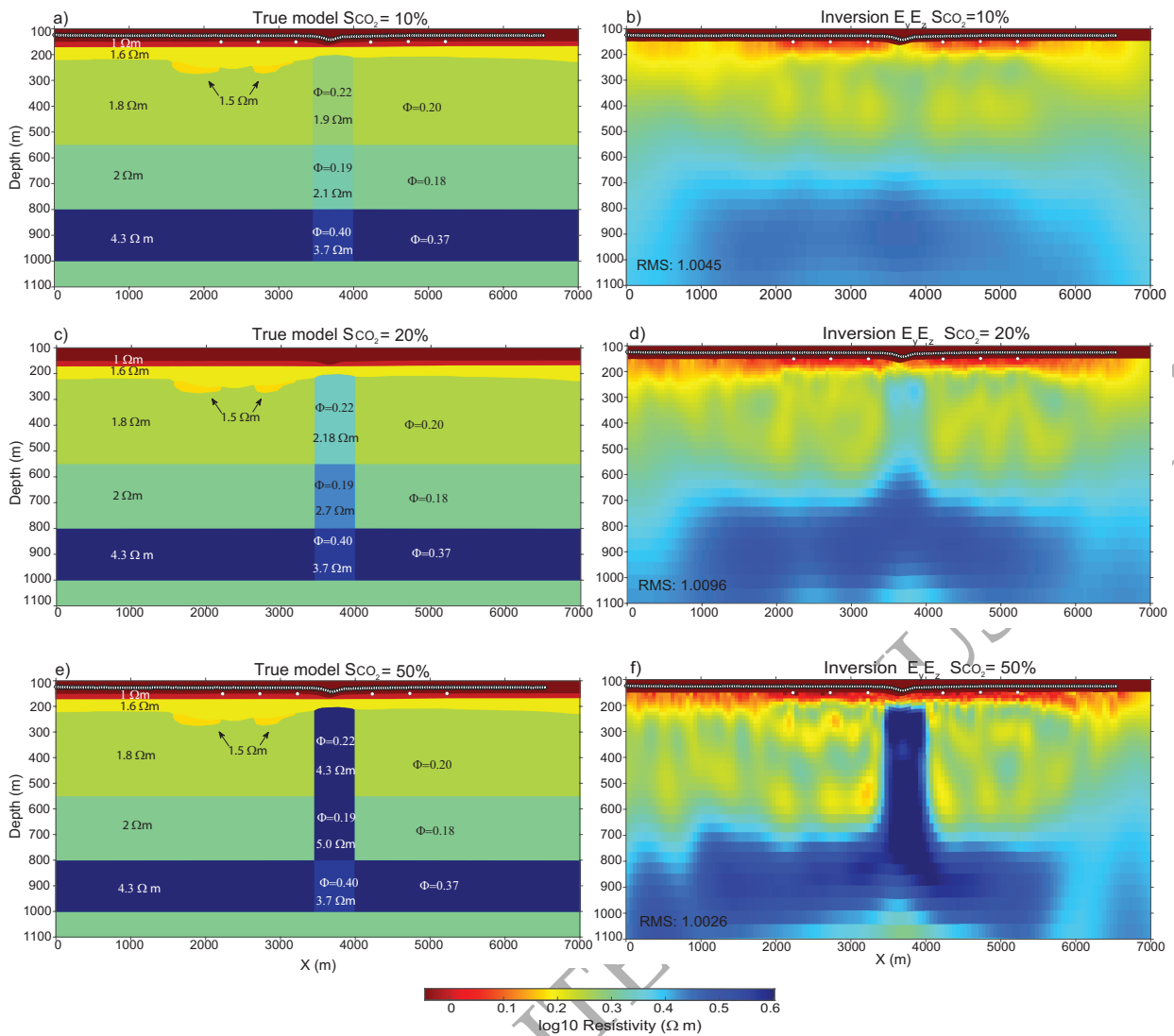
Figure 12. True synthetic resistivity models and resulting resistivity sections from inversion using both E_y and E_z data. Three different scenarios of CO_2 leakage from the reservoir into the chimney are the true model with the chimney saturated with 10 per cent CO_2, c) the true model with the chimney saturated with 20 per cent CO_2 and e) the true model with chimney saturated with 50 per cent CO_2. In the second columns b), d), and f) is the resulting resistivity sections from a simultaneous E_y and E_z component inversion for the three scenarios (10, 20, and 50 per cent CO_2 leakage in the chimney).
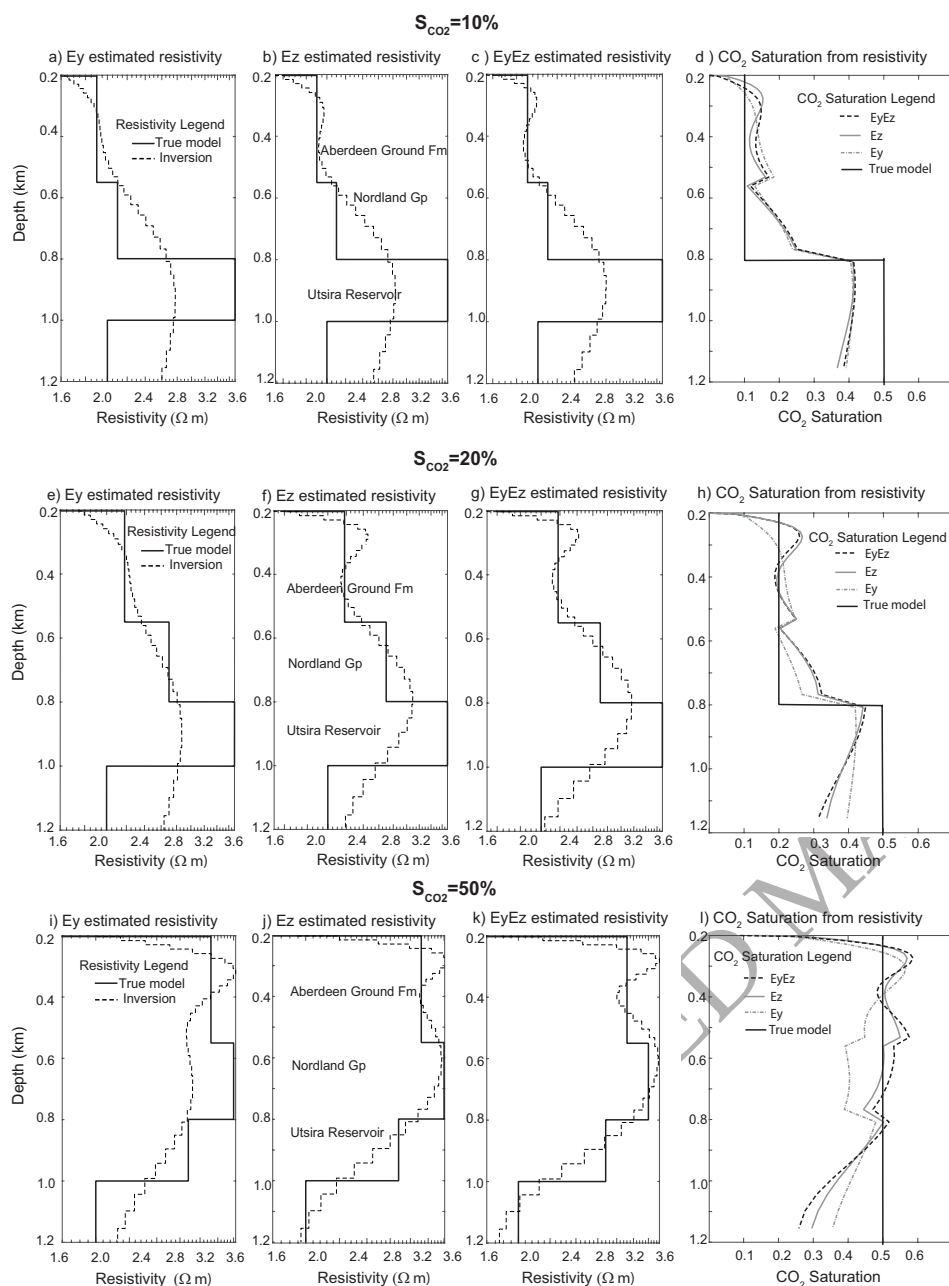
Figure 13. Resistivity profiles and CO_2 saturation at the chimney (2D model distance = 3.8 km) for separate E_y, E_z and simultaneous E_y and E_z inverted resistivity results (black dashed line) against the true resistivity model (solid black line) for the three CO_2 leakage scenarios (10, 20 and 50 per cent). E_y only inverted resistivity profiles are in the first column with the chimney saturated with a)10 per cent CO_2, with e)20 per cent CO_2, and with i)50 per cent CO_2. The second column are the E_z only inverted resistivity profiles for the same three scenarios: b)S_{CO2}= 10 per cent , f)S_{CO2}= 20 per cent and j)S_{CO2}= 50 per cent . In the third column are the simultaneous E_y E_z inverted resistivity profiles for the same three scenarios: c) S_{CO2}= 10 per cent, g) S_{CO2}= 20 per cent and k)S_{CO2}= 50 per cent. Finally, the fourth column is the predicted CO_2 saturations derived from the inverted resistivity models and rock physics relationships (See section 3.1). The true CO_2 saturations (black solid line) are plotted along with predictions from the three data types: E_y (grey dotted line), E_z (grey solid), and joint E_y and E_z (black dashed line) for d)S_{CO2} 10 per cent, h)S_{CO2} 20 per cent and l)S_{CO2} 50 per cent.

log10 Resistivity (Ω m)
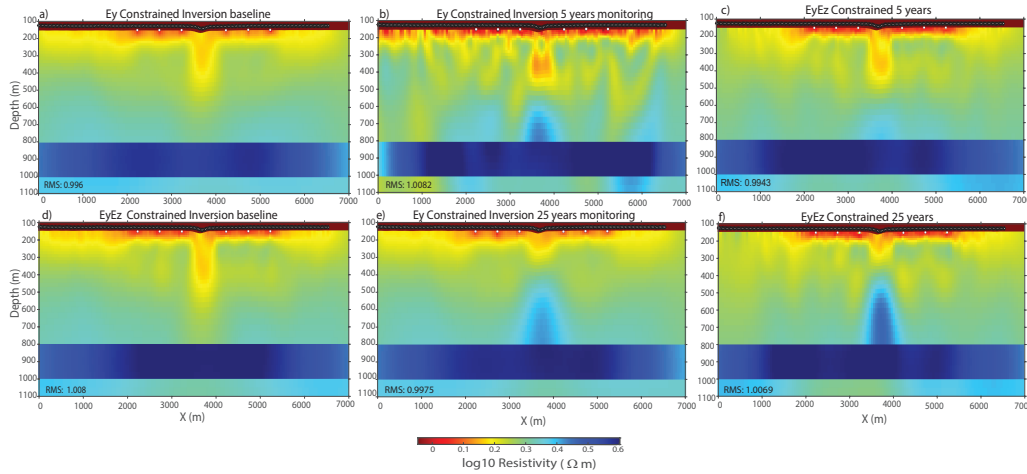
Figure 14. Resistivity inversion for the baseline and the two scenarios with gradational CO_2 saturation in the chimney representing different times after CO_2 injection, corresponding to Figure 4. The same geometry, data range, and properties of the STEMM-CCS survey line 2 are used in modelling. In the top row the resistivity inversions, constrained by the reservoir top and base using E_y for the baseline model (Figure4a) in a); E_y for the model with leakage through the chimney after 5 years of CO_2 injection (Figure4b) in b); E_y E_z for the model with leakage through the chimney after 5 years of CO_2 injection in c). In the second row there are the inverted resistivity sections, constrained by the reservoir top and base using: $E_y E_z$ for the baseline model (Figure4a) in d);using E_y for the model with leakage through the chimney after 25 years of injection (Figure4c) in e) and E_y E_z for the model with leakage through the chimney after 25 years of CO_2 injection (Figure4c) in f)

Table 1. Archie's and Waxman-Smits input parameters for WG, Witch Ground Formation; CP, Coal Pit Formation; LB, Ling Bank Formation; AG, Aberdeen Ground Formation; NG, Nordland Group seal; UF, Utsira Formation (injection reservoir). Table modified from Marín-Moreno et al. (2019)

Layer	Thickness[ad]	ϕ [bc]	T[e]	ρ_w[f]	a [hi]	m[gh]	BQ$_v$[j]	CEC [h]	n[k]
Seabed	-	-	7°C	0.2777 Ωm	-	-	-		
WGF	23 m	0.44	7.69 °C	0.2733 Ωm	0.9	1.8	0.0748	0.05	-
CPF	37 m	0.34	8.8 °C	0.2665 Ωm	0.9	1.8	0.1757	0.05	-
AGF	300 m	0.2	17.8 °C	0.2218 Ωm	0.9	1.8	4.5	-	2
NG	440 m	0.18	31 °C	0.1995 Ωm	0.9	1.8	4.5	-	2
UF	200 m	0.35	37 °C	0.1781 Ωm	1.1	1.6	-	-	1.8

[a] Judd et al. (1994) for WG, CP and AG

[b] Paul & Jobson (1991) for WG and CP

[c] Audigane et al. (2007) and [d]Chadwick et al. (2004) for AG, NG and UF

[e] Temperature at seabed Shell-UK-limited (2014) and 30°C/Km Harper (1971)

[f] Seawater resistivity from North Sea (STEMM-CCS) CSEM transmitter CTD data Gehrmann et al. (2021b)

[g] For WGF, CPF and AGF Riedel et al. (2006) and Falcon-Suarez et al. (2021)

[h] For NG seal and UF Falcon-Suarez et al. (2018)

[i] For WG, CP, AG and NG Mavko et al. (2009)

[j] Calculated from Equation A.14 with ϕ_{sh}=0.1 (Audigane et al. 2007) and V_{SH}=0.8 (Chadwick et al. 2002)

[k] Alemu et al. (2013)

Table 2. Resistivity of the partially brine saturated formations (Gas models) within the chimney: WGF, Witch Ground Formation; CPF, Coal Pit Formation; LBF, Ling Bank Formation; AGF, Aberdeen Ground Formation; NGS, Nordland Group seal; UF, Utsira Formation (Reservoir).

| | | outside chimney | | | within chimney | | | | |
| | | $\rho_0^{(1)}$ | $\rho_0^{(2)}$ | | $\rho_t^{(1)}$ | $\rho_t^{(2)}$ | ρ_t | ρ_t | ρ_t |
Layer	ϕ	$S_w=1$	$S_w=1$	ϕ_c	$S_w=1$	$S_w=1$	$S_{CO_2}=0.1$	$S_{CO_2}=0.2$	$S_{CO_2}=0.5$
WGF[*]	0.44	1 Ωm	1 Ωm	-	-	-	-	-	-
CPF[*]	0.34	1.6 Ωm	1.6 Ωm	-	-	-	-	-	-
AGF	0.2	1.8 Ωm	1.8 Ωm	0.22	1.5 Ωm	1.5 Ωm	1.81 Ωm	2.18 Ωm	4.3 Ωm
NGS	0.18	2Ωm	2 Ωm	0.19	1.8 Ωm	1.8 Ωm	2.1 Ωm	2.7 Ωm	5.0 Ωm
UF	0.37	1 Ωm	4.0 Ωm	0.40	0.9 Ωm	3.7 Ωm[3]	3.7 Ωm[3]	3.7 Ωm[3]	3.7 Ωm

[*]formations with no fractures as the chimney does not extend up to these layers. A porosity 10 per cent lower is assumed at the chimney from the AG up to the Utsira formation.

(1)background model, 100 per cent saturated with brine before CO_2 injection

(2)background model, 100 per cent saturated with brine in the seal after injection

(3)Utsira formation 50 per cent saturated with CO_2

APPENDIX A: ELECTRICAL RESISTIVITY MODELLING FOR SAND AND CLAY-RICH SEDIMENTS

The empirical relationship proposed by Archie (1942) relates physical rock and fluid properties to the bulk (matrix+fluid) electrical resistivity for clean sand through two empirical relationships (Equations A.1 and A.2)

$$F = \rho_0/\rho_w = a\phi^{-m} \tag{A.1}$$

$$\frac{\rho_t}{\rho_0} = \left(\frac{\phi^m \rho_t}{a\rho_w}\right) = S_w^{-n} \tag{A.2}$$

From which:

$$S_w = \left(\frac{a\rho_w}{\phi^m \rho_t}\right)^{1/n} \tag{A.3}$$

F is known as the formation factor, given by the resistivity ratio of the bulk fully saturated formation (ρ_0) and pore water resistivity (ρ_w). The second relationship relates the electrical resistivity of a partially saturated formation ρ_t with water saturation S_w, porosity ϕ, tortuosity factor a saturation exponent, n and cementation factor m.

The tortuosity factor a is an empirical constant close to 1 (Mavko et al. 2009). The saturation exponent n depends on the type of fluids, with values close to 2 for gas-water systems (Mavko et al. 2009). For unconsolidated sand, m varies depending on the shape of the sediments and increases from 1.3 to 1.9 with decreasing grain size and sphericity (Falcon-Suarez et al. 2021).

In order to correct the effect of clay on the formation resistivity, the original Archie's equation is commonly modified by adding a conductivity term X to account for the excess conductivity (Mavko et al. 2009):

$$\frac{1}{\rho_t} = \frac{S_w^n}{F\rho_w} + X \tag{A.4}$$

In the Waxman and Smits (1968) modification the term X is defined in the following equation:

$$\frac{1}{\rho_t} = \frac{S_w^n}{F\rho_w} + \frac{S_w^{n-1}BQ_v}{F} = \frac{S_w^n \phi^m}{a\rho_w} + \frac{S_w^{n-1}BQ_v\phi^m}{a} \tag{A.5}$$

depending on Q_v, the cation exchange capacity per unit pore volume (meq/m^3) and B is the equivalent conductance of the clay (Na$^+$) exchange cations.

$$Q_v = \frac{CEC(1-\phi)D_o}{\phi} \tag{A.6}$$

where CEC is the cation exchange capacity and D_0 is the mineral grain density of the shale.

There have been several expressions developed for B since the original paper from Waxman and Smits (1968). Juhasz (1981) gives the following expressions for B, with T as the temperature in °C:

$$B = \frac{-1.28 + 0.225T - 4.059 \times 10^{-4}T^2{}^{1.23}}{1 - \rho_w}(0.045T - 0.27) \tag{A.7}$$

Isolating the resistivity ρ_t for partially brine saturated formation:

$$\rho_t = [\frac{a\rho_w}{\phi^m S_w^n (1 + \frac{\rho_w}{B} Q_v} S_w)]$$ (A.8)

The brine saturation S_w can be obtained from these models by solving (Bilodeaux, 1997):

$$S_w = [\frac{a\rho_w}{\rho_t} \phi^m (1 + \rho_w B Q_v / S_w^{n-1})]^{1/n}$$ (A.9)

For n=2 the explicit solution (ignoring the negative root) is:

$$S_w = \sqrt{\frac{a\rho_w}{\rho_t} \phi^m (1 + \rho_w B Q_v / S_w^{n-1})}$$ (A.10)

The normalized Waxman–Smits equation from Juhasz (1981) removes the need for CEC being measured from cores as it uses V_{SH} (volume of shale) derived from well-logs (e.g. gamma ray or density-neutron) to estimate Q_v, obtained as follows:

$$Q_{vn} = \frac{Q_v}{Qv_{sh}} = \frac{V_{SH}\phi_{sh}}{\phi}$$ (A.11)

where ϕ_{sh} is the total shale porosity and Q_{vn} is the normalized Q_v, which is in fact the shale-water saturation expressed in terms of the fraction total pore space, ranging from 0 in clean sand to 1 in clay. ρ_{wsh} is the shale water resistivity for 100 per cent brine-saturated 'shaly' or 'clay-rich' formation identified with the aid of the gamma-ray or V_{SH} log. This value is chosen from the resistivity well log. Similarly, BQ_v is normalized with the shale response and written in terms of Q_{vn} and since BQv_{sh} is the difference between apparent shale water conductivity ($1/\rho_{wsh}$) and formation water conductivity ($1/\rho_w$. BQ_v can be written in terms of formation water resistivity (ρ_w) and shale resistivity (ρ_{sh}) as follows:

$$BQ_v = Q_{vn}BQ_{vsh} = Q_{vn}(\frac{1}{\rho_{wsh}} - \frac{1}{\rho_w}) = \frac{V_{SH}\phi_{sh}}{\phi}(\frac{F_{sh}}{\rho_{sh}} - \frac{1}{\rho_w})$$ (A.12)

The normalized Waxman–Smits-Juhasz equation of Juhasz (1981) is obtained from substituting Equation A.12 in the Equation A.5, resulting in:

$$\frac{1}{\rho_t} = \frac{S_w^n}{F\rho_w} + \frac{V_{SH}\phi_{sh}}{\phi}(\frac{F_{sh}}{\rho_{sh}} - \frac{1}{\rho_w})\frac{S_w^{n-1}}{F}$$ (A.13)

and simplifying,

$$\frac{1}{\rho_t} = \frac{S_w^n \phi^m}{a}[\frac{1}{\rho_w} + \frac{V_{SH}\phi_{sh}}{\phi}(\frac{a}{\rho_{sh}}\phi_{sh}{}^m - \frac{1}{\rho_w})S_w^{-1}]$$ (A.14)

APPENDIX B: ARP'S LAW

The pore water resistivity ρ_w within the sediments is calculated using Arp's empirical relationship Arps (1953). Arp's Law extrapolates the pore water resistivity from a known pore water resistivity and temperature to any given depth using the geothermal gradient (Arps 1953; Collett & Ladd 2000).

$$\rho_w^{T2} = \rho_w^{T1} \frac{T_1 + 21.5}{T_2 + 21.5} \tag{B.1}$$

where ρ_w is the brine solution resistivity, T_1 and T_2 is the corresponding temperature at top and bottom layers. The pore water resistivity per layer was computed iteratively down the model per layer starting with the water resistivity at the seabed of 0.2777 Ωm measured from the CTD and the North Sea seabed annual average temperature of $7°$ from Shell-UK-limited (2014). This is consistent with the temperature measured by the CTD at 20-40 m above the seabed of 7.7 $°$. The Temperature of each layer was determined using these starting parameters, Arp's Law, and the North Sea geothermal gradient of $30°$ C Km^{-1} Harper (1971). All input values are presented in Table 7.
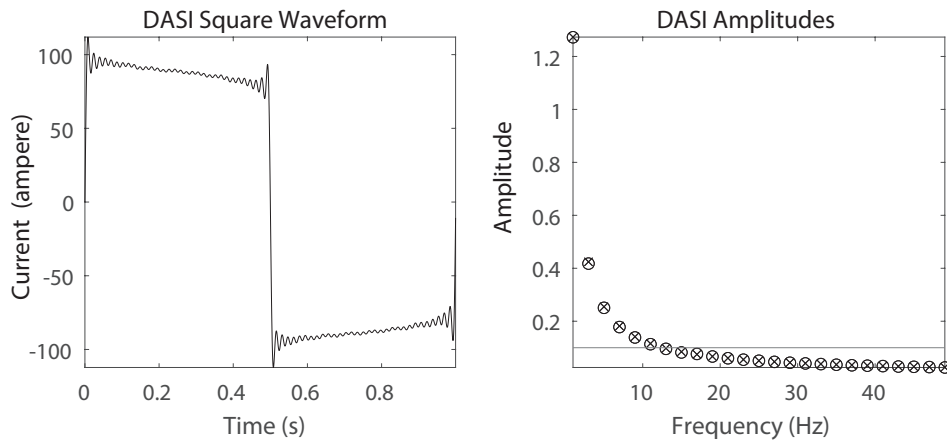
Figure A1. A 100 A square waveform with 1 Hz fundamental frequency was transmitted by DASI during the Scanner pockmark survey (left). The normalized waveform time series is Fourier transformed to get the amplitude for the fundamental and harmonic frequencies (filled circles) compared with an ideal 1 Hz square wave (x). Frequencies whose amplitudes are below 0.1 of peak current (below horizontal line) have low signal strength.

## APPENDIX C: FREQUENCY SELECTION

(STEM-CCS). As such the frequency selection was guided by analysing the square wave transmitted during this survey (Figure A1). Frequencies above 11 Hz (from 13-60 Hz) were disregarded for the 2D modelling by looking at the amplitude attenuation at each harmonic frequency and selecting 0.1 as the amplitude (peak current) cut-off, as shown in Figure A1.
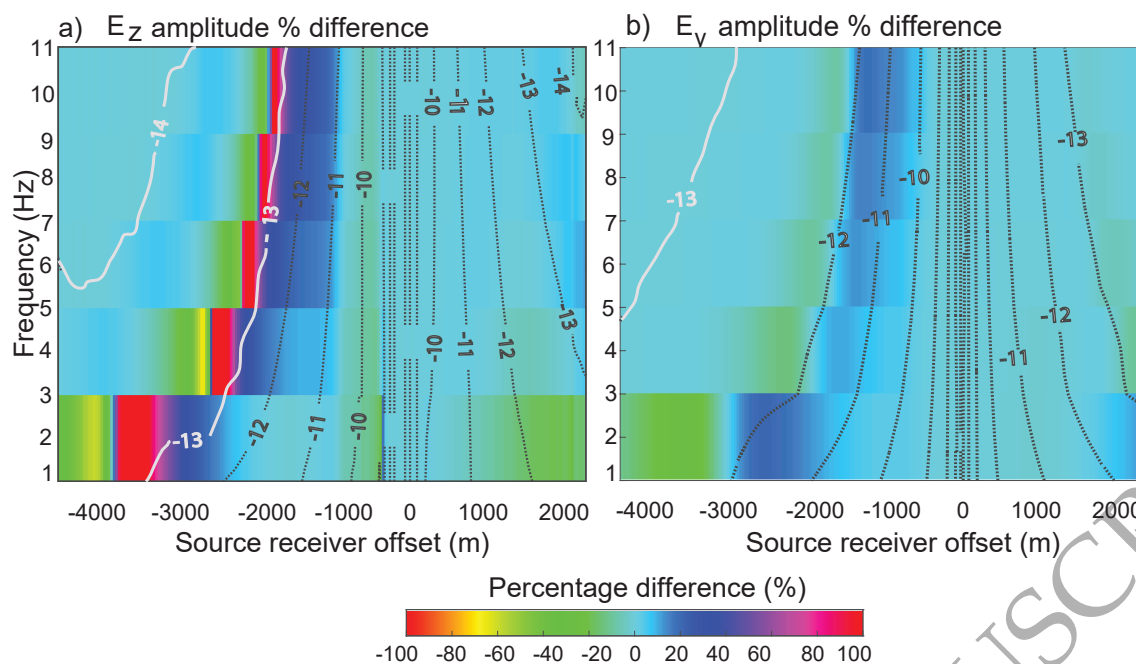
Figure A2. Amplitude percentage difference between two models: a chimney with S_{CO_2}=0 per cent and a chimney with S_{CO_2}=10 per cent for E_z a) and E_y b). This amplitude anomaly (percentage difference) for the 2D model with S_{CO_2}=10 per cent is calculated for a receiver 1000 m from chimney (OBE-D). Dotted black contours correspond to the $\log_{10}$ electric field amplitude (model with a chimney). The STEMM-CCS instrument noise floor at 10^{-13} V/Am^2, contours below noise floor marked with a continuous white line. Color represents the percentage difference.

## APPENDIX D: ANOMALY OF A CHIMNEY SATURATED WITH 10 PER CENT CO$_2$

We calculate the anomaly of a chimney saturated with 10 per cent CO_2 in comparison with the scenario of a chimney with no CO_2, in order to analyse the detectability of a chimney with 10 per cent CO_2 after injection. Figure A2 shows the amplitude percentage difference plot between the model with a chimney saturated with brine from base to top (Figure 3b) and a model saturated with 10 per cent CO_2 (Figure 3c), for receiver OBE-D and the 6 frequencies modelled (1-11 Hz). For both E_z and E_y, the anomaly for the chimney at the fundamental frequency (1 Hz) is very narrow, only present at the higher source-receiver offset between 2000-3000 m. For the higher frequencies (3-11 Hz) the E_z anomaly is of higher percentage difference (25-40 per cent) than the anomaly in E_y (10-20 per cent). The error modelled was 4 per cent and similar to what was observed in the STEMM-CCS CSEM data from the North Sea.
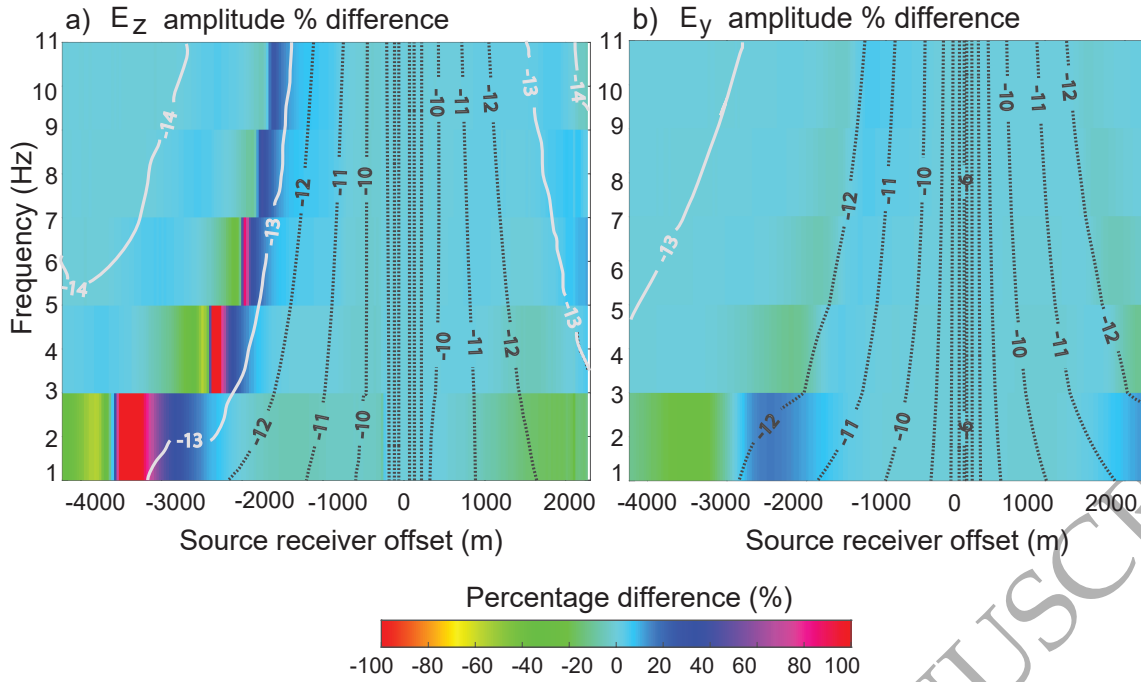
Figure A3. Amplitude percentage difference between two background models: the chimney with S_{CO_2}=10 per cent and the model with no chimney for E_z a) and E_y b). This amplitude anomaly (percentage difference) for the 2D model with S_{CO_2}=10 per cent is calculated for a receiver 1000 m from the chimney (OBE-D). Dotted black contours correspond to the $\log_{10}$ electric field amplitude of the model with a chimney. The STEMM-CCS instrument noise floor at 10^{-13} V/Am^2, contours below noise floor marked with a continuous white line. Color represents the percentage difference.

APPENDIX E: ANOMALY OF A SEAL WITH NO CHIMNEY AND A CHIMNEY SATURATED WITH 10 PER CENT CO$_2$

With the purpose of analysing the anomaly of a 10 per cent saturation chimney in comparison with the background sediments Figure A3 shows the amplitude percentage difference between the model with no chimney (Figure 9a), where only the host geology is modelled, and a model with a chimney saturated with 10 per cent CO$_2$ (Figure 3c), for receiver OBE-D and the 6 frequencies modelled (1-11 Hz). For both E_z and E_y there is a minor amplitude anomaly above the noise floor for the whole frequency band (1-11 Hz). There is a very narrow anomaly in E_y at 1-3 Hz. The E_z and E_y anomaly is in the range of 0-10 per cent percentage difference. In this study, we believe this scenario is not detectable, as we have modeled data with 4 per cent Gaussian error.
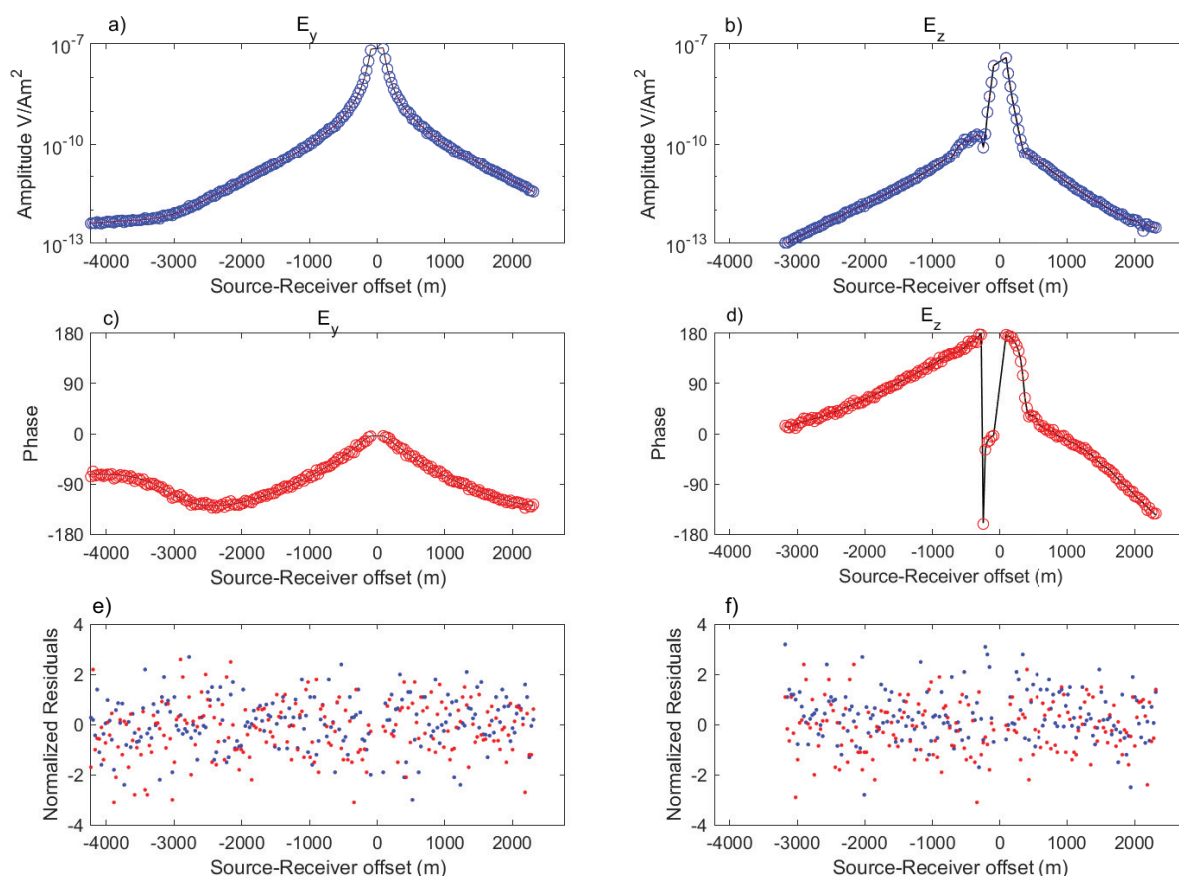
Figure A4. The 1 Hz amplitude response (top-(a) and (b)), phase (middle-(c) and (d)) response and normalized residuals (bottom -(e) and (f)) of a 2D model before injection (no chimney) is shown for the synthetic forward modelled data (circles) and the resulting inverted data (solid black line) for E_y (left (a),(c),(e)) and E_z (right (b),(d),(f)) versus source-receiver offset at OBE-D.

APPENDIX F: SYNTHETIC DATA AND INVERSION EXAMPLE

Figure A4 below shows an example of electric field data for an ocean bottom instrument (OBE) at a fundamental frequency of 1 Hz. The airwave affects the E_y component and is observed from ∼3100 m source-receiver (Tx-Rx) offset and beyond. This is recognized due to the phase flattening and a more gradual amplitude decay. It is expected that for this offset, sensitivity to the resistivity structure of the seabed will be reduced (Constable 2010). However, for our study, the chimney signal is expected at offsets <3100 m, as can be seen in Figure 8.